POLITECNICO
MILANO 1863

SCUOLA DI INGEGNERIA INDUSTRIALE
E DELL'INFORMAZIONE

High Mobility in Ge Quantum Wells: Hall Bars Characterization for Semiconductor Qubits

Tesi di Laurea Magistrale in
Engineering Physics - Ingegneria Fisica

Author: **Luca Nardelli**

Student ID: 252349
Advisor: Prof. Daniel Chrastina
Co-advisors: Prof. Giovanni Isella, Dr. Stefano Calcaterra
Academic Year: 2025-26

Abstract

In the last few years, the scientific community has made a significant effort to develop disruptive quantum technologies. However, despite some exciting results, no real breakthrough in the implementation of the qubit has been reached. A promising realization is based on a two dimensional carrier gas, hosting two electrostatically defined coupled quantum dots. This implementation is characterized by a very high coherence time and good integration with classical hardware.

The purpose of this thesis is the characterization of Ge/SiGe heterostructures confining a two dimensional hole gas. Analysis has been conducted at very low temperatures (down to $4K$) and high magnetic fields (up to $7.5T$), on Hall bars fabricated on the heterostructures. Critical fabrication steps have been deeply characterized, in particular the Atomic Layer Deposition and Etching processes. Different figures of merit have been extracted from the heterostructures.

Abstract in lingua italiana

Recentemente, il computer quantistico è diventato un importante oggetto di ricerca nella comunità scientifica per via delle varie applicazioni che può offrire. Eppure, nonostante alcuni risultati promettenti, non si è mai affermata una tecnologia definitiva per l'implementazione di qubit. Una realizzazione promettente è quella formata all'interno di un gas bidimensionale di portatori, dove si trovano due quantum dot accoppiati. Questa realizzazione è caratterizzata da alti tempi di coerenza e una buona integrazione nell'hardware attuale.

L'obiettivo di questa tesi è la caratterizzazione di eterostrutture di Ge/SiGe, le quali sono ottime per confinare un gas bidimensionale di lacune. Le analisi sono state condotte su barre di Hall a basse temperature (fino a $4K$) e alti campi magnetici (fino a $7.5T$). Gli step di fabbricazione più importanti sono stati largamente caratterizzati, in particolare gli step di Atomic Layer Deposition e Etching. I valori di diversi parametri delle eterostrutture sono stati ottenuti.

List of Figures

1.1 Quantum dot fabricated on a Ge quantum well stack. Adapted from IST Austria [1]. . . . 4
1.2 Typical HMOS stack grown at L-NESS and analyzed in this work. 5
1.3 The historic evolution of the 2DHG mobility in the group IV semiconductors at low temperatures [2]. . . . 6
1.5 Isoenergy surfaces for the energy dispersion of HH and LH in bulk Ge. Different values of $\frac{\partial^2 E}{\partial k^2}$ corresponds to different directions, so that the final mass tensors are anisotropic. . . . 9

2.1 Elastic scattering model representation. The scattering event between the state $\vec{k_i}$ and $\vec{k_f}$ can be completely described by the vector $\vec{q}$. . . . 12
2.2 Difference between unscreened (a) and screened (b) elastic scattering phenomena. One can observe how the screening provided by other electrons decreases the overall scattering angle. . . . 13
2.3 Fit of the mobility-density experimental data in a SiGe conduction channel due to different scattering mechanisms. The effect of each mechanism is shown separately [3]. . . . 16

3.1 Qualitative behavior of ρ_{xx} and ρ_{xy} when a single carrier is present. . . . 21
3.2 Mobility spectra calculated on synthetic data featuring two carrier gases of low mobility (Adapted) [4]. . . . 22
3.3 Simulation of the DOS function when an external magnetic field is applied. No broadening (top) or gaussian broadening (bottom) are considered. . . . 25
3.4 Weak localization regime. One can see the sudden decrease as the magnetic field moves from 0. . . . 27
3.5 SdH oscillations and QHE measured on a similar HMOS respect to the structures analyzed in this work. Adapted from [5]. . . . 28
3.7 Simulation of the DOS function at high magnetic field ($B = 5T$). . . . 30

4.1 LEPECVD reactor setup scheme. . . . 33
4.2 Stack of the HMOS samples analyzed in this work. . . . 34

4.3 Stack of the highly strained Ge channel analyzed in this work. 35
4.4 Hall bar representation. One can observe both the body and legs of the bar, as well as the w and l values from which the geometrical ratio is obtained. 36
4.5 CAD drawn litographic mask for a gated Hall bar designed for this work. One can see the close-up to a leg of the Hall bar, revealing a region where no gate has been deposited to avoid overlap with the contact pad. 37
4.6 Final lithographic masks used on the samples. Hall bars have been (a) scaled and (b) rotated respectively. 38
4.7 Hall bar fabrication process flow. The representation shows a cross-section of the device, taken at the leg point of the Hall bar. 39
4.8 Different resist profiles depending on resist type. 40
4.9 Oxide spectra taken thanks to a J.A. Woollam VASE Ellipsometer. The spectra were fitted according to a multilayer model using the tabulated optical constants of Si, Ge and Al_2O_3 while leaving the thickness of the layers as free parameters. 41
4.10 SEM image taken on the edge of the Hall bar pad. One can see the etching profile, as well as the oxide adhesion to the stack. The layer appears to be perfectly conform to the HMOS, even on the vertical wall formed by the etching step. A zoom on the wall is shown to see the etching profile created. Out of the 260 nm target depth, only 120 nm have been etched. Furthermore, the Ge QW has been laterally etched more than the corresponding $Si_{0.3}Ge_{0.7}$ layer, creating an indentation in the wall profile. 42
4.11 SEM image taken on the body of the Hall bar. One can see both the gold and the oxide layers, as well as the etching profile. From the image, it is really hard to predict the thickness of the oxide layer in this region. 43
4.12 Comparison between extracted data with a Savitzky-Golay method and a moving mean method. One can see that the latter is way more instable and produces a result that globally has not a mean value of 0. 45
4.13 FFT analysis of the HMOS SdH oscillations at different temperatures. Extracted from the data represented in Figure 4.12. 47
4.14 Example of a Ge/SiGe HMOS percolation density analysis [6]. Starting from the measurements of μ for different values of n_H taken by changing V_g (left), one can then calculate $\sigma(n_H)$ and plot the corresponding curve (right). The red line is the theoretical fit with the (2.23). 48

5.1 Schematic figures of a Hall bar, with enumerated contact pads and the current flowing from pads 1-4. The Hall bar analysis will always refer to these numbered contacts, with the 7th pad simply not present in the case of the oxide-no-gate Hall bars. 49
5.2 Stack of the 11607 channel region. 50
5.3 Different Hall bar structures analyzed in the 11607 sample. (a) A part of the Hall bar leg is left uncovered. (b) the leg contact is completely onto the Hall bar leg. (b) Only the gate metal is deposited onto a part of the legs to avoid freeze-out. (d) SEM image of the sample 11608 device. 51
5.4 Resistance as a function of temperature as the sample was cooling down, measured between contact 2-3. An area around $T = 35K$ can be indicated as the freeze-out region of the conducting channel (in this case, the substrate). 52
5.5 Stack of the 11608 sample channel region. 52
5.6 11608 Hall bar gate leakage between contacts 4-7, represented in a $I(V)$ curve. One can see the perfect ohmic $I(V)$ line typical of metal conduction. 53

6.1 Stack of the 11585 channel region 55
6.2 11585 Hall bar body conduction (contact 1-4) represented in a $I(V)$ curve. 56
6.4 Channel current (contacts 1-4) and gate current (contacts 1-7) for different values of V_g. Initially, the channel current seems to follow the gate current, before they separate more for $V_g > -1.35$ V. 56
6.5 Stack of the 11586 channel region. 57
6.6 Channel current (contacts 1-4) and gate current (contacts 1-7) in sample 11586 at $T = 300$ K. 58

Contents

Abstract i

Abstract in lingua italiana ii

List of Figures iii

Contents vii

Introduction 1

1 Ge/SiGe Heterostructures 3
- 1.1 Heterostructures in quantum dots . . . 3
- 1.2 Ge/SiGe Heterostructures . . . 5
- 1.3 Band structure . . . 7
- 1.4 Effective mass anisotropy . . . 7

2 Transport Theory 11
- 2.1 Transport theory . . . 11
- 2.2 Scattering mechanisms . . . 14
  - 2.2.1 Local impurities scattering . . . 14
  - 2.2.2 Remote impurities scattering . . . 15
  - 2.2.3 Interface roughness . . . 15
  - 2.2.4 Alloy scattering . . . 16
- 2.3 Freeze-out . . . 16
- 2.4 Percolation density . . . 17

3 Magnetic Field Effects 19
- 3.1 Conductivity Tensor . . . 19
- 3.2 Hall Effect . . . 20
- 3.3 Two Carrier Model . . . 22

3.4 Scattering magnetoresistance . . . 23
3.5 Quantum treatment . . . 23
3.6 Weak localization . . . 26
3.7 Shubnikov-De Haas Effect . . . 27
3.8 Quantum Hall Effect . . . 28
3.8.1 Fractional Quantum Hall Effect . . . 29
3.9 Spin splitting . . . 30

4 Experimental Techniques **33**
4.1 LEPECVD . . . 33
4.2 Samples . . . 34
4.3 Hall bars . . . 35
4.4 Fabrication . . . 35
4.4.1 Patterning of metallic contacts . . . 37
4.4.2 Definition of the Hall bars . . . 39
4.4.3 Deposition of the oxide . . . 40
4.4.4 Deposition of the gate and finishing steps . . . 42
4.5 Cryostat . . . 43
4.6 Methods and analysis . . . 44
4.6.1 ρ_{xx} and ρ_{xy} analysis . . . 44
4.6.2 FFT Analysis . . . 46
4.6.3 Percolation density . . . 47

5 Highly Strained Ge Samples Analysis **49**
5.0.1 11607 sample . . . 49
5.0.2 11608 sample . . . 52

6 Ge/SiGe HMOS Samples Analysis **55**
6.0.1 11585 Oxide no Gate . . . 55
6.0.2 11585 Gated . . . 56
6.0.3 11586 gated . . . 57

Conclusions **59**

Bibliography **61**

Introduction

In recent years, quantum technologies have started to become more important as they have introduced the world to the so-called second quantum revolution. One of the most important aspects of this revolution is quantum computing: exploiting quantum information carriers (normally referred to *qubits*) to compute very hard problems, where the parallelism that quantum computation features can be exploited as much as possible. Many different technologies have been studied in order to create a good qubit, and a very promising implementation is represented by two coupled quantum dots, creating a two-level quantum system that works as a logic gate. This type of qubit could be hosted in a heterostructure that contains a two-dimensional carrier gas. The advantage of this realization is the very long coherence time and, when fabricated with elements of the IV group like Si or Ge, its good integration with classical hardware [7, 8, 9].

The scope of this thesis is to characterize various Ge/SiGe heterostructures transport properties, as well as to define a manufacturing workflow at L-NESS (Laboratory for Nanostructure Epitaxy and Spintronics on Silicon, Politecnico di Milano) to fabricate Hall bars for the characterizations. The interest comes from the ability of Ge/SiGe heterostructures to confine a two-dimensional hole gas (2DHG), which makes them a good candidate for hosting a qubit. The heterostructure studied in this work is a HMOS (heterostructure metal oxide semiconductor) made of a strained Ge quantum well (QW) cladded by two barrier layers of SiGe. Lastly, a gate is deposited to influence the transport properties of the well. HMOS have been grown at L-NESS by a Low Energy Plasma Enhanced Chemical Vapor Deposition (LEPECVD) reactor while part of the Hall bars have been fabricated with the help of the Institute of Science and Technologies, located in Klosterneuburg, Austria. The remaining devices have been manufactured in Polifab, the clean-room facility of Politecnico di Milano. A characterization has been conducted on the manufacturing process, to deeply understand the critical steps of the realization of the devices. Particular attention has been given to the Atomic Layer Deposition (ALD) and the Etching processes.

The transport properties of 2DHG have been studied on the Hall bars thanks to a cryostat capable of reaching temperatures of 4 K and equipped with a magnetic field generator

capable of reaching 7.5 T. In these conditions, the classical Hall effect can be observed, as well as quantum phenomena such as the Shubnikov–de Haas (SdH) oscillations and the Quantum Hall Effect (QHE). From these measurements, one can obtain several figures of merit regarding the materials used for the HMOS. In this regime, the Hall effect and the Quantum Hall effect can be observed, also thanks to the geometry of the devices. The cryostat made it possible to work at temperatures down to 4 K. In addition, a supercoiled magnetic field generator was used to generate fields up to 7.5 T.

For each sample, different quantities can be extracted from the measurements taken within the cryostat. Mobility, carrier density, effective mass, Dingle ratio, critical density, and Fermi level have all been obtained when possible.

In the first part of this thesis, the physical phenomena are discussed, starting from the description of transport and scattering and finishing with the effect of an applied magnetic field.

In the second part, the reader can find all the methods and instruments that have been used to grow and fabricate the structures, as well as their characterization. In this part, one can also find all the methods used to measure and extract the parameters for transport characterization.

In the third part, the discussion of all the analyzed samples is presented, with an important focus on the effective mass, Dingle ratio, and mobility.

1 | Ge/SiGe Heterostructures

1.1. Heterostructures in quantum dots

In the last decade, quantum computing has been a dominant research field around the world. Creating high performance qubits has proven to be quite a challenge, so different approaches have been studied throughout the years, i.e. Josephson junction qubits, photonic qubits, and Nitrogen-Vacancy (NV) centers [7, 10, 11, 12, 13].
In this scenario, *coupled spin* quantum dots represent an important option due to their high stability and long coherence time. This is only possible due to the low scattering rate and high mobility these structures present, so their performance is tied to the quality of the material platform[8]. In addition, compatibility with standard semiconductor manufacturing processes that they exhibit is very important [9]. The possibility of using already existing process lines can be a huge factor in the development and diffusion of the technology.
A possible implementation of a quantum dot consists of a heterostructure-MOS (HMOS) and a confining gate on top [14], which can be electrically biased. Then, by injecting a current, one can tunnel electrons into the dot or remove the charges from it, thereby creating control over the device. The choice of the HMOS used is very important, and much progress has been made in the last 30 years.
The first realization of a controlled coupled spin qubit dates back to 2005, when a GaAs/AlGaAs HMOS structure demonstrated an average relaxation time of up to $T_2^* \sim$ 10 ns, with a manipulation time on the order of hundreds of picoseconds. Additionally, an extended spin coherence time has been measured, revealing a $T_2^* \sim 1\mu$s [15]. A later implementation used Si/SiO_2 structures, showing significant improvements in coherence time T_2^* that increased to 100μs, with an increment of manipulation time in the order of microseconds. [16].
The first realization of Si/SiGe quantum dots was in 2014, when the research team achieved promising results on coherence time in the device [17]. This type of HMOS has demonstrated high mobility and very low scattering rates, reaching a dephasing time of $T_2^* \sim 40\mu$s.

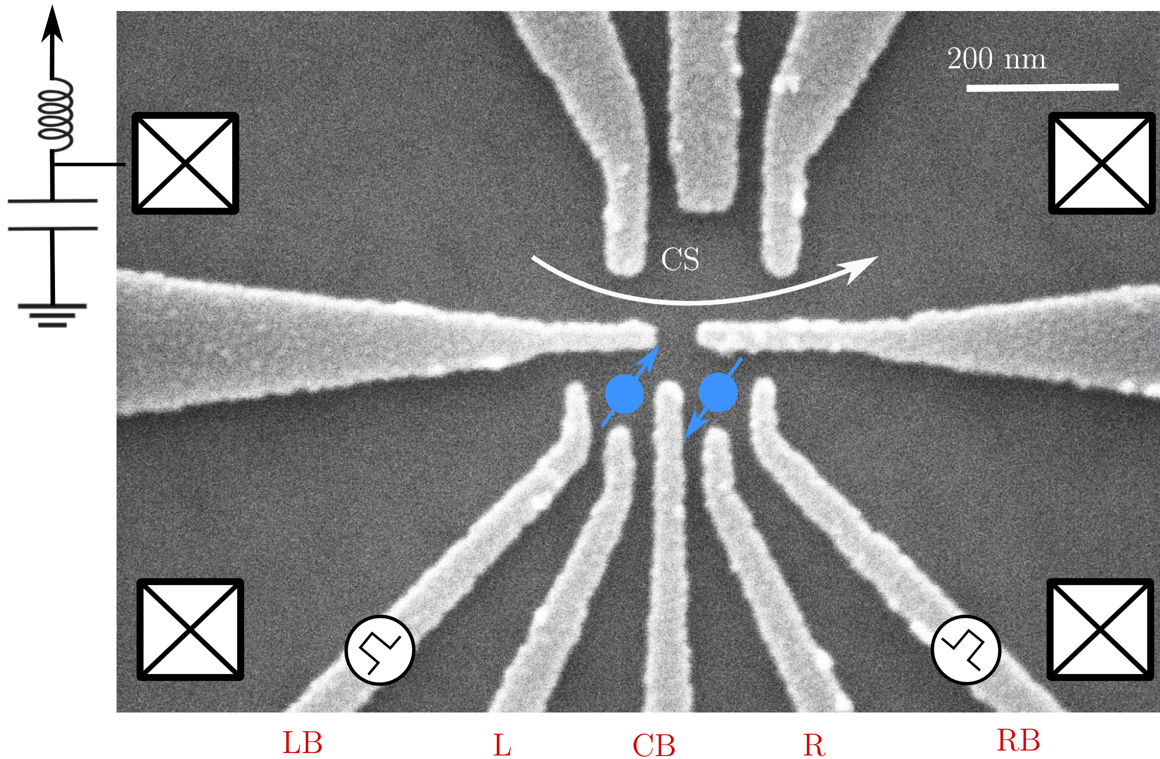

Figure 1.1: Quantum dot fabricated on a Ge quantum well stack. Adapted from IST Austria [1].

Since then, ISTA has been trying to implement qubits in germanium heterostructures, since the large spin-orbit coupling allows for fast manipulation times [1]. In order to do so, heterostructures were grown at L-NESS, then sent to ISTA to create Hall bars and qubit devices. The Hall bars were sent back to L-NESS for magnetotransport characterization. Those steps were necessary, as L-NESS did not have access to the Atomic Layer Deposition (ALD) technique, which is a critical step of the Hall bars fabrication process to deposit the gate oxide.

Because of this, the scope of this work was to create and test a manufacturing process to produce Hall bars directly at L-NESS, thanks to the collaboration with Polifab, which recently acquired an ALD tool. Moreover, both Hall bars fabricated in Polifab and highly strained Ge devices fabricated in ISTA have been characterized to investigate Ge transport properties.

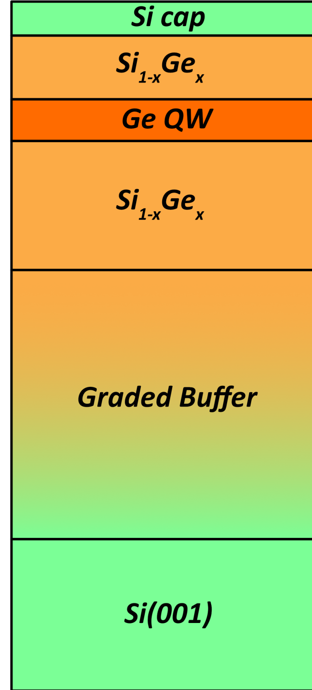

Figure 1.2: Typical HMOS stack grown at L-NESS and analyzed in this work.

1.2. Ge/SiGe Heterostructures

Recently, increasing interest has been shown in undoped heterostructures, as they have demonstrated high 2D carrier mobility at low temperatures [18, 19]. Those results have also been observed in the case of modulation doped heterostructures; however, doping introduces gate leakage, charge noise, and device instability at low temperatures. Therefore, they are not suitable for creating reliable qubit implementations [20, 21].
In this scenario, the Ge/SiGe heterostructure seems promising for creating high-quality quantum dots for quantum computing.

The manufacturing process of Ge/SiGe heterostructures is challenging due to the lattice mismatch between the two materials. On one hand, this can introduce strain, which can be engineered to control the energy bands in the well. On the other hand, it may also relax on the interface, introducing defects that may reduce the mobility in the sample [22]. Then, the main challenge is to choose the right composition of the SiGe layers, in order to influence the energy bands but avoiding relaxation within the well.

This section aims to describe a typical SiGe heterostructure as analyzed in this work. [8, 22, 23]. The process starts from an unintentionally doped (ρ = 1–10 Ω·cm) Si(001)

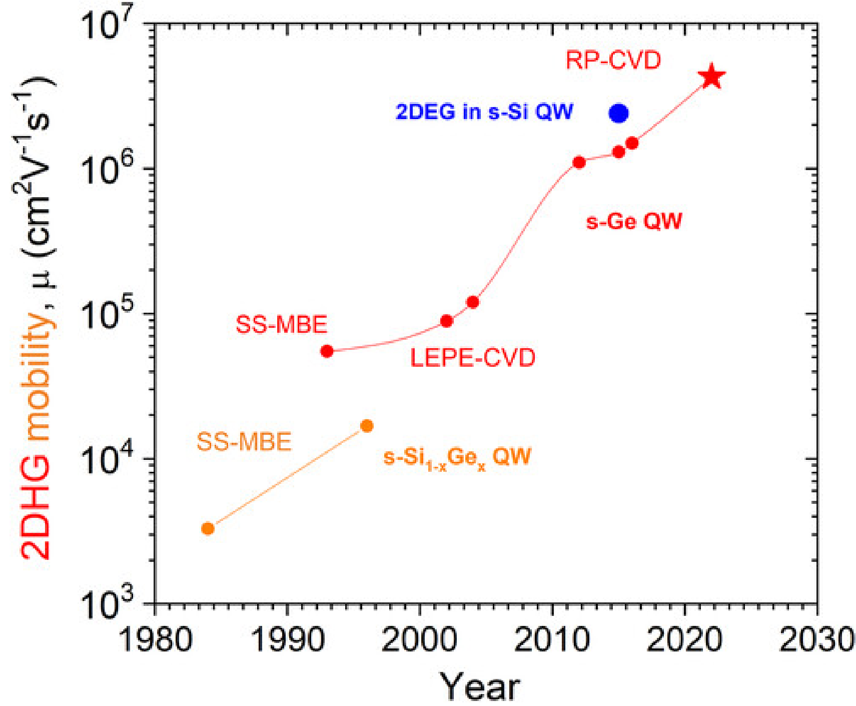

Figure 1.3: The historic evolution of the 2DHG mobility in the group IV semiconductors at low temperatures [2].

wafer. On top of Si, a graded buffer (GB) is grown: this consists of a micrometers-thick $Si_{1-x}Ge_x$ layer where the Ge content increases linearly at a rate of 7%/μm.
The virtual substrate (VS), a thick, constant composition layer that matches the final composition of the GB, is then grown to achieve full relaxation. The deposition rate is then slowed from 5 nm/s to 0.5 nm/s to gain more control over the thickness, and a spacer of several hundreds of nanometers matching the VS composition is deposited. After that, the pure Ge *quantum well* (QW), also called *channel*, is grown. As a result of Nextnano simulations [24], the QW layer thickness has to be around 20 nm, in order for the confinement to be effective.
Then another constant composition layer of $Si_{1-x}Ge_x$ is grown to form the upper barrier of the QW. Lastly, a thin sacrificial Si cap is grown so that native oxidation creates a stable SiO_2 layer, which can be easily removed with HF treatment.

Typically, SiGe HMOS structures are characterized by a sheet density n_s ranging from 2×10^{10} cm^{-2} up to 1×10^{12} cm^{-2}, with a mobility around $\sim 1 \times 10^6$ cm^2/V·s[25]. Recently, better results have been reached, lowering the effective mass in these systems to around $0.05 m_e$ with a barrier Ge concentration up to $x = 0.75$ [26]. Thanks to these improvements, mobility has reached $\mu \sim 7 \times 10^6$ cm^2/(Vs)[27, 28].

1.3. Band structure

The heterostructure forms a QW in the Ge layer as a result of the difference in the energy gap of the two materials. The energy gap in Ge is, in fact, smaller than that of Si, creating an offset in both the conduction and valence bands. This is a good setup for creating a band structure known as a *Type-II band alignment*, which is characterized by having band edges lower (in the case of the conduction band) than those of both barriers. This creates carrier confinement in a small energetic region, as shown in Figure 1.4a. Due to the geometry of the QW, holes and electrons are confined in different bands [29].[30]. It should be noted that this confinement is only in the growth direction (assumed to be the z direction), while carriers are free to move in the xy plane. There are different ways to bend and change the rectangular energy diagram of the QW. Levels can be shifted by applying a potential through a metal gate on top of the HMOS or by doping the $Si_{0.3}Ge_{0.7}$ layers: the first case is particularly interesting, as it can be externally controlled to modulate the bands. Furthermore, it does not introduce any impurity in the structure, which can be a huge limit in the case of doped structures. Tuning the bias, a triangular quantum well can appear in the growth direction, as indicated in Figure 1.4b [23].
The triangular well can be described by the Fang-Howard wavefunction [31, 32]:

$$\Psi_0(z) = \left(\frac{b^3}{2}\right)^{1/2} z \exp\left(-bz/2\right) \tag{1.1}$$

b can be written as:

$$b = \left[\frac{12 m_z e^2}{\hbar^2 \varepsilon_r \varepsilon_0}\left(n_{Depl} + \frac{11}{32} n_s\right)\right]^{1/3} \tag{1.2}$$

where $n_D epl$ is the density of ionized impurities and m_z is the effective mass in the z direction. From this band structure, one can expect an accumulation behavior at the Ge-$Si_{0.3}Ge_{0.7}$ interface, where, if a metal layer is present, the density of holes can be tuned by the voltage applied to the gate.

1.4. Effective mass anisotropy

In a semiconductor, an effective mass tensor is commonly used to describe the $E(k)$ relation in different directions. The mass can be split into 3 different components, namely m_x, m_y and m_z. This representation shows the effective mass anisotropy [34], which strongly influences the conduction properties of the material in different directions. This

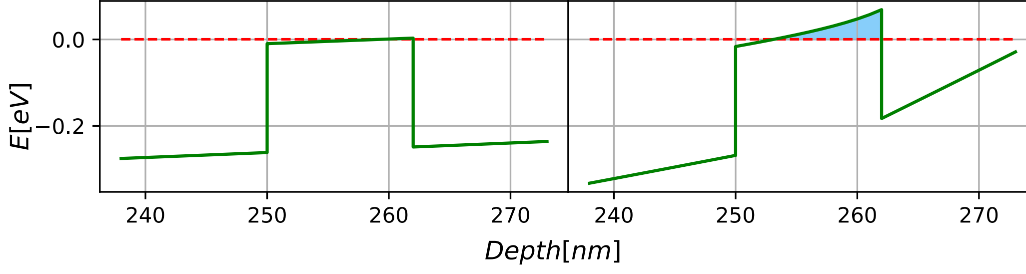

(a) Nextnano simulation of the band diagram of a $Si_{0.3}Ge_{0.7}/Ge/Si_{0.3}Ge_{0.7}$ structure, with a constant n-doping $N_d = 10^{15}$ cm^{-3} and a gate bias of $V_g = -0.3$ V (left) and $V_g = -2.1$ V (right). As the bias increases, an accumulation behavior can be observed in the blue area near the interface.

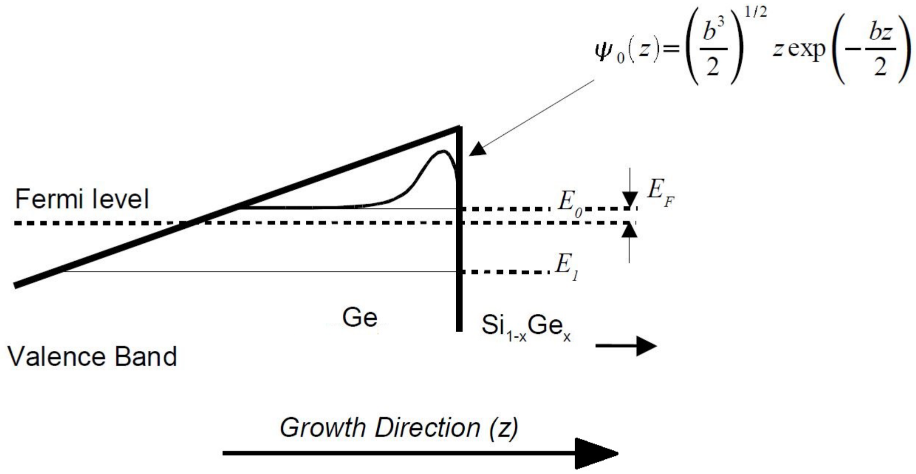

(b) Shape of the Fang-Howard wavefunction in a triangular [33].

is directly proportional to the shapes of the conducting orbitals, so that different shapes of isoenergy surfaces (Figure 1.5) correspond to different values of m^* components.

In HMOS, different phenomena can change the behavior of light holes (LH) and heavy holes (HH) masses with respect to bulk Ge.
The first consideration is about confinement [35, 36]. Because of the presence of the QW, two pairs of states in the degenerate point Γ emerge, corresponding to HH states and LH states, with the first being more strongly bound. This effect enhances the *mass inversion* phenomena in the xy plane, where:

$$m_{HH}^{xy} < m_{LH}^{xy} \tag{1.3}$$

In order to consider the additional effect of strain, the Luttinger Hamiltonian can be used in the $k \cdot p$ model [37]. The results show that the in-plane mass becomes abruptly lighter as tensile strain is generated in the system. This can be explained by the p_x and p_y orbitals

coming closer together, decreasing the m_x and m_y values.
These two effects work cooperatively to enhance HH in-plane conduction, allowing high mobility to be achieved in the xy plane of the sample.

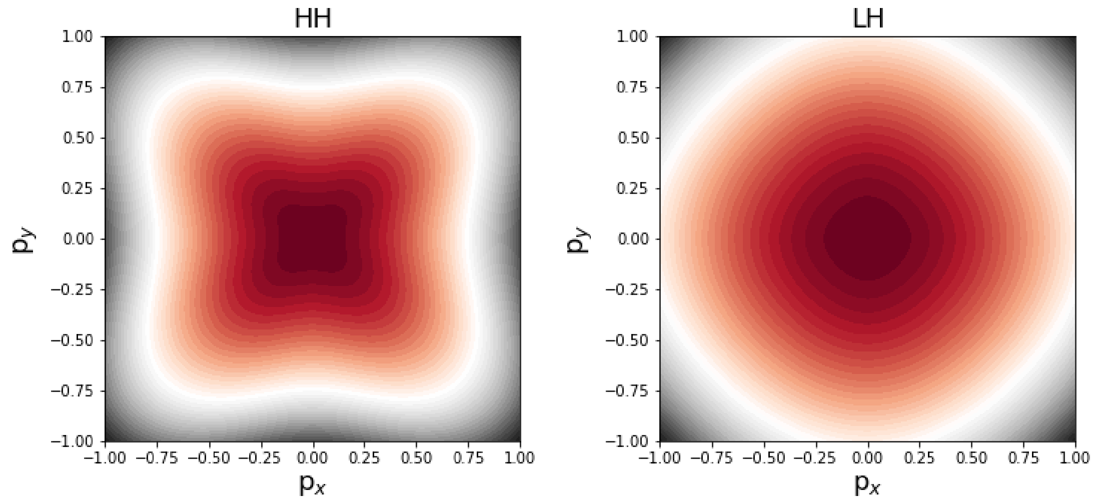

Figure 1.5: Isoenergy surfaces for the energy dispersion of HH and LH in bulk Ge. Different values of $\frac{\partial^2 E}{\partial k^2}$ corresponds to different directions, so that the final mass tensors are anisotropic.

2 | Transport Theory

2.1. Transport theory

One of the most important parameters for describing the conduction in a material is mobility μ, which can be defined as:

$$\mu = \frac{|\vec{v}|}{|\vec{E}|} \tag{2.1}$$

Where $\vec{v}$ is the velocity of the carriers and $\vec{E}$ is the drift electric field that drives the current. From this quantity, one can retrieve the resistivity of the material with electron concentration n_e:

$$\rho = \frac{1}{en_e\mu} \tag{2.2}$$

Using Drude's model, μ can be rewritten as:

$$\mu = \frac{e\tau_{tr}}{m^*} \tag{2.3}$$

Where τ_{tr} is the transport lifetime. The total transport lifetime can be obtained using Matthiessen's rule:

$$\frac{1}{\tau_{tr,tot}} = \sum_{i=1} \frac{1}{\tau_i} \tag{2.4}$$

Where τ_i are the transport lifetimes for all the i independent scattering mechanisms within the system. Note that if we have a correlation between different τ_i, the formula is no longer valid unless a correlation is added term [38]:

$$\frac{1}{\tau_{tr,tot}} = \sum_{i=1} \frac{1}{\tau_i} + \frac{1}{\tau_{couple}} \tag{2.5}$$

It is important to introduce some hypotheses for the model:

- All scattering mechanisms are independent of one another. This condition puts the $\tau_{couple} \to \infty$ in the (2.5).
- The Fermi surface is circular in the conduction plane. This is a good assumption, even if the HH band is slightly anisotropic (see Figure 1.5).
- All scattering mechanisms are elastic, which means $|\vec{k_i}| = |\vec{k_f}| = |\vec{k_F}|$, where $\vec{k_F}$ is the Fermi vector. Thanks to this approximation, one can consider all scattering events to change only the direction of the wavevector, and not its modulus.

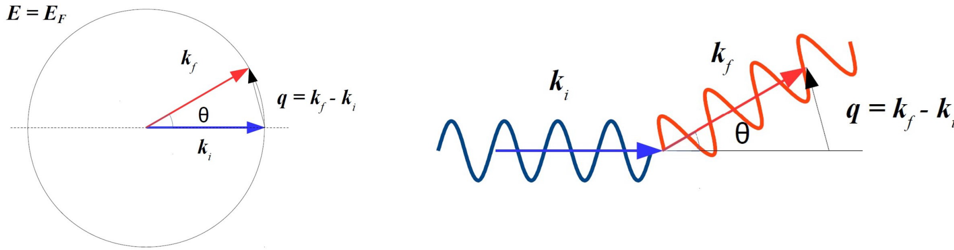

Figure 2.1: Elastic scattering model representation. The scattering event between the state $\vec{k_i}$ and $\vec{k_f}$ can be completely described by the vector $\vec{q}$.

A scattering vector can be defined $\vec{q}$:

$$|\vec{q}| = |\vec{k_f} - \vec{k_1}| = 2k_F \sin\frac{\theta}{2} \tag{2.6}$$

in which the angle θ is the angle between $\vec{k_i}$ and $\vec{k_f}$.

It is important to introduce the concept of *scattering matrix element* $V(q)$ which describes the scattering energy depending on the value of q. All scattering mechanisms can be described by this matrix, the most common ones will be treated in section 2.2.

One can also write the equations for τ_{tr} and τ_q, where the latter is called *quantum scattering lifetime*. They can be obtained by integrating $V(q)$ over all the possible scattering angles, with some additional terms in order to consider directionality and screening:

$$\tau_{tr,i} = \frac{m^*}{\pi\hbar^2}\int_0^\pi (1-\cos\theta)\frac{|V_i(q)|^2}{\varepsilon_q^2}d\theta \tag{2.7}$$

$$\tau_{q,i} = \frac{m^*}{\pi\hbar^2}\int_0^\pi \frac{|V_i(q)|^2}{\varepsilon_q^2}d\theta \tag{2.8}$$

The main difference between the two equations is the $(1-\cos\theta)$ term, which is not

present for τ_q. In fact, quantum scattering can be considered isotropic under a certain critical angle θ_c, while transport scattering has a directionality that can be related to the scattering angle [39].

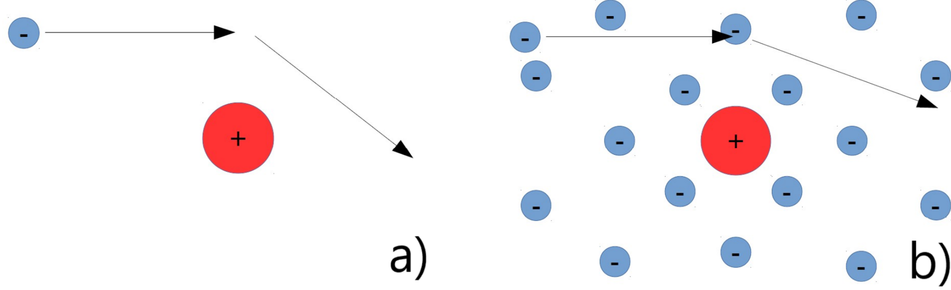

Figure 2.2: Difference between unscreened (a) and screened (b) elastic scattering phenomena. One can observe how the screening provided by other electrons decreases the overall scattering angle.

Another important element in the integrals is ε_q, named *Static Polarization Function*. It gives the ability to also consider screening phenomena, where the presence of other electrons screens the scattering centers and decreases the overall scattering angle (Figure 2.2). A good model for describing ε_q is the Thomas-Fermi theory, which form in 2D is:

$$\varepsilon_q = 1 + \frac{q_s}{q} \tag{2.9}$$

$$q_s = \frac{m^* e^2}{2\pi\varepsilon_r\varepsilon_0\hbar^2} \tag{2.10}$$

thanks to the long wavelength limit [40, 41].

Another important quantity to describe the scattering phenomena is the *Dingle ratio*, defined as:

$$\alpha = \frac{\tau_{tr}}{\tau_q} \tag{2.11}$$

Its value can be taken as an indication of the nature of the scattering potentials [42]. For short-range isotropic scattering $\alpha \sim 1$, while for long range Coulomb scattering τ_{tr} is typically larger, leading to α being much larger than 1.

2.2. Scattering mechanisms

There exist different types of scattering mechanisms, which are all defined by a different scattering matrix $V(q)$. The general equation for $V(q)$ is the following:

$$V(q) = n_i \int e^{-iq\cdot r} v(r) d^2 r \tag{2.12}$$

Where n_i is the density of impurities and $v(r)$ is the impurity potential. It is also convenient to introduce the concept of *form factor*, which is a correction factor that takes into account the charge distribution of the 2DHG.

From experimental data, it appears that all scattering phenomena have a dependence on temperature such that:

$$\mu = T^{-\gamma} \tag{2.13}$$

Note that the value of γ does not directly correlate with the dominant scattering mechanism [43]. In this analysis, only some low-temperature scattering mechanisms will be discussed in order to better understand their characteristics.

2.2.1. Local impurities scattering

Local impurity scattering is caused by dopants localized between the Ge channel and the SiGe layer. The scattering matrix element is the following [3]:

$$|V(q)|^2 = n_i \left(\frac{e^2}{2\varepsilon_0 \varepsilon_r q} \right)^2 \frac{1}{(1 + q/b)^6} \tag{2.14}$$

Where b is defined by (1.2), and the form factor can also be expressed by an exponential decrease [40]:

$$F = e^{-qd} \tag{2.15}$$

Where d is the distance between the impurity and the electrons. This shows how local impurities cause strong scattering in the material, even though the typical density is far lower than that of remote impurities.

2.2.2. Remote impurities scattering

Remote impurity scattering is caused by the high density of donors at the interface. The scattering matrix can be written as [44]:

$$|V_{ri}|^2 = n_D \Gamma_D(q) D(q) \left(\frac{e^2}{2\varepsilon_0 \varepsilon_r q} \right)^2 \tag{2.16}$$

where n_D is the doping sheet density. $\Gamma_D(q)$ can be expressed as

$$\Gamma_D(q) = \frac{[1 - \exp(-2qW)] \exp(-2qS)}{2qW} \tag{2.17}$$

With W being the thickness of the doped region and S the *setback distance* between the channel and the SiGe layer. $\Gamma_D(q)$ represents the donor form factor and has a sharp peak at $q = 0$, which contributes significantly to τ_q but not to τ_{tr}.
$D(q)$ is also present in (2.16), representing a correlation correction between events. At small q, it can be written as

$$D(q) \approx \left(\frac{W^2}{12} + \Delta^2 \right) q^2 \tag{2.18}$$

Where the Δ value represents the random fluctuations in the spacing between donors. This type of scattering has a huge impact on mobility in SiGe HMOS.

2.2.3. Interface roughness

Interface roughness scattering arises from the presence of carriers near the Si-Ge interface. It can be modeled as Gaussian scattering [45]:

$$|V(q)|^2 = \pi \Delta_0^2 \Lambda^2 \exp\left(-\Lambda^2 q^2/4\right) \tag{2.19}$$

Where Λ and Δ_0 are, respectively, the width and height of the roughness. As the carrier density increases, the effect of interface roughness also increases due to the presence of more carriers near the surface. Generally, this type of scattering has minor effects on a semiconductor heterointerface.

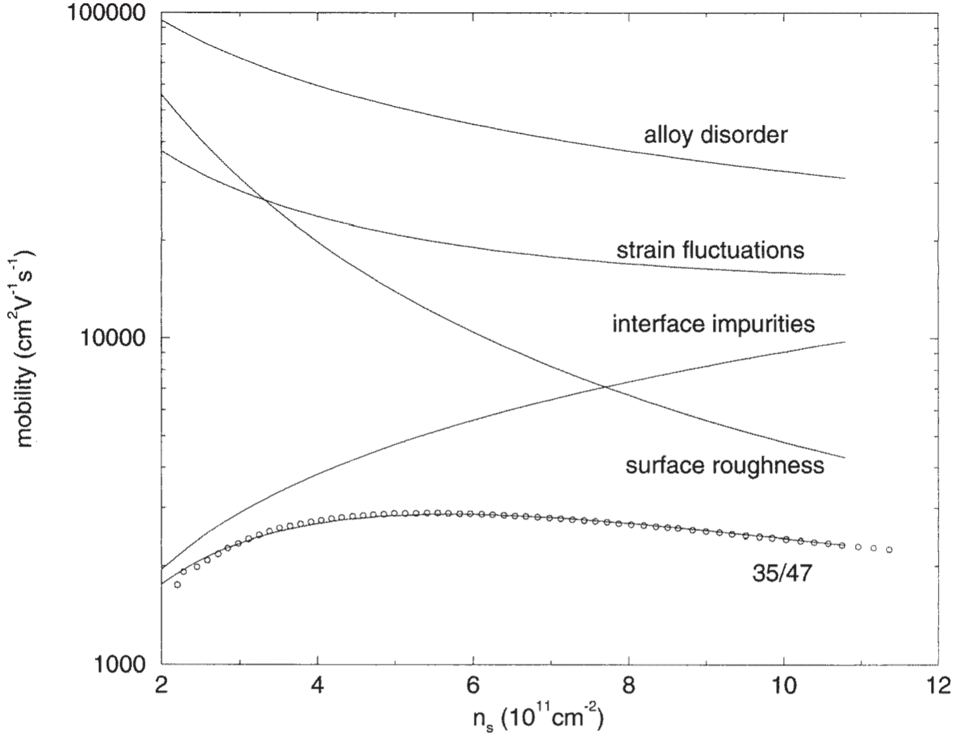

Figure 2.3: Fit of the mobility-density experimental data in a SiGe conduction channel due to different scattering mechanisms. The effect of each mechanism is shown separately [3].

2.2.4. Alloy scattering

Alloy scattering is caused by the random positions of the Si and Ge atoms inside the crystal structure. Its scattering matrix can be generalized as [46]:

$$|V(q)|^2 = x(1-x)\Omega_0 \delta E^2 \frac{3b}{16} \tag{2.20}$$

where Ω_0 is the unit cell volume, δE represents the intensity of the interaction, and b has been defined in (1.2). This type of scattering is absent in the case of pure Ge or Si channels.

2.3. Freeze-out

When a semiconductor is cooled to very low temperatures, a freeze-out phenomenon can occur, which corresponds to a large decrease of the carrier population and the material becoming unable to conduct. This is because the generation of electron-hole pairs and the ionization of dopants both depend on temperature.

In any semiconductor, the intrinsic concentration of electrons due to the thermal genera-

tion of pairs can be written as [47]:

$$n_e = n_h = 2\left(\frac{k_B T}{2\pi\hbar^2}\right)^{3/2}(m_e m_h)^{3/4}\, e^{-E_g/(2k_B T)} \tag{2.21}$$

Where E_g is the intrinsic energy gap of the semiconductor. One can see that as the temperature goes down, the exponential term decreases and drastically decreases the intrinsic concentration.

In the case of an extrinsic semiconductor, i.e. an n-doped semiconductor, one also has to consider the donor electrons:

$$N_d - n_d = \frac{N_d}{1 + 2e^{(E_d - E_F)/k_B T}} \sim n_e \tag{2.22}$$

Where N_d is the donor concentration, n_d is the donor-bounded electron concentration, and E_d is the donor energy. Note that, generally, at low temperatures, the generation of electron-hole pairs is so low that almost all the carriers are provided by the donors. This is normally referred to as the *saturation* regime.

At even lower temperatures, the energy is so low that almost all donors cannot ionize, and in Equation 2.22 the electron concentration drops, as indicated in Figure 2.4b. This condition is called *freeze-out* regime and makes the value of ρ in Equation 2.2 increase abruptly.

2.4. Percolation density

The percolation density is an important figure of merit for studying the 2D Metal Insulator transition (2D-MIT). This behavior is typical of 2D materials with high mobility and low density, i.e. $n_p \sim 10^9$ cm^{-2} in Si [48]; It can be described as a carrier density-driven change in the dependence of ρ on T. In particular, the transition from a metallic behavior regime ($n > n_p$, $\frac{d\rho}{dT} > 1$) to an insulating behavior regime ($n < n_p$, $\frac{d\rho}{dT} < 1$) [**?**]. Note that in samples with high disorder, the value of n_p can be significantly higher, up to $n_p \sim 10^{12}$ cm^{-2}, as electrons become localized even at high densities [49]. In order to electrically characterize the system, one can write the conductivity σ as:

$$\sigma \approx (n - n_p)^p \tag{2.23}$$

where p is the *percolation exponent*. Theoretically, its value is set to be 1.31. It has been found that p also has a dependence on T, which can be neglected only at very low temperatures [50]. An example of these properties can be seen in Figure 2.4a.

Since the percolation density describes the disorder in SiGe heterostructures, a low value of n_p is crucial for the stability of quantum dots, especially the ones working very close to the 2D-MIT. Recently, a percolation density of 4.5×10^9 cm^{-2} has been reached in a Ge/SiGe HMOS, indicating a very low disorder and consequently high mobility in the sample [27].

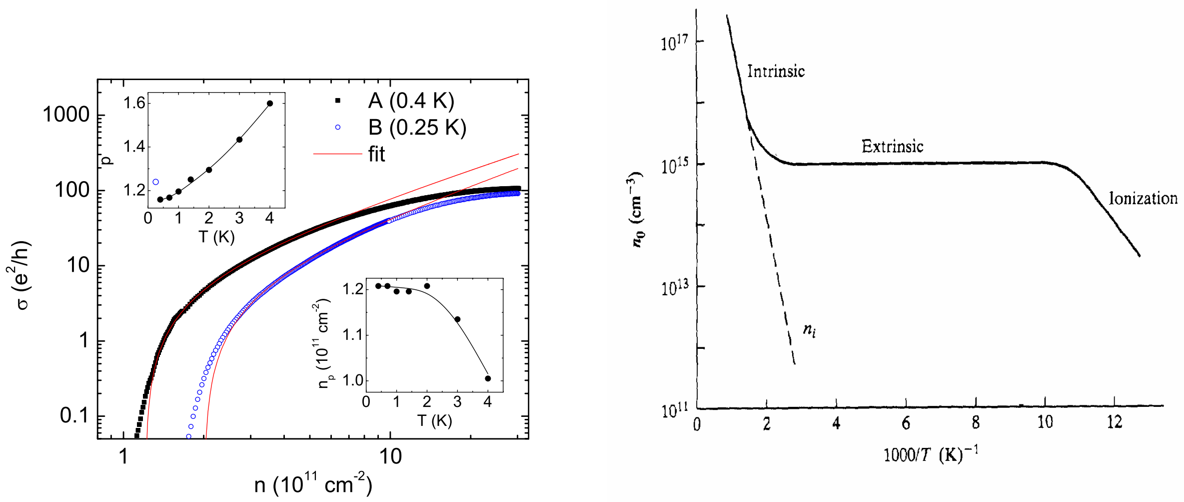

(a) Percolation density in a 2DEG Si MOSFET [?]. In the main plot, σ is plotted at $T = 0.4$ K and $T = 0.25$ K. Note how both n_p and p have a dependency on temperature.

(b) Carrier concentration at different temperatures [51]. At low temperatures, one can see the sudden decrease of carriers from the stationary (saturation) regime.

3 | Magnetic Field Effects

3.1. Conductivity Tensor

Ohm's law describes the proportionality between current density $\vec{J}$ and electric field $\vec{E}$. In its most general form, it can be written as [47]:

$$\begin{pmatrix} J_x \\ J_y \end{pmatrix} = \begin{pmatrix} \sigma_{xx} & \sigma_{xy} \\ \sigma_{yx} & \sigma_{yy} \end{pmatrix} \begin{pmatrix} E_x \\ E_y \end{pmatrix} \tag{3.1}$$

$$\vec{J} = \bar{\bar{\sigma}} \vec{E} \tag{3.2}$$

Where $\bar{\bar{\sigma}}$ is the *conductivity tensor*. It can be demonstrated that $\sigma_{xx} = \sigma_{xy}$ and $\sigma_{xy} = -\sigma_{yx}$. it is also possible to express the *resistivity tensor* as the inverse of the conductivity tensor:

$$\bar{\bar{\rho}} = \bar{\bar{\sigma}}^{-1} \tag{3.3}$$

$$\bar{\bar{\rho}} = \begin{pmatrix} \rho_{xx} & \rho_{xy} \\ -\rho_{xy} & \rho_{xx} \end{pmatrix} = \frac{1}{\sigma_{xx}^2 + \sigma_{xy}^2} \begin{pmatrix} \sigma_{xx} & \sigma_{xy} \\ -\sigma_{xy} & \sigma_{xx} \end{pmatrix} \tag{3.4}$$

Note that also $\bar{\bar{\rho}}$ diagonal terms are equal and the antidiagonal terms are opposite.

Introducing the conductivity and resistivity tensors allows for the description of the directionality of resistance in conduction, which is fundamental to understanding the Hall Effect.

3.2. Hall Effect

In this section, a classical treatment of the Hall Effect will be presented, in the so-called weak field limit $\omega_c\tau \ll 1$, where:

$$\omega_c = \frac{eB}{m^*} \tag{3.5}$$

ω_c is called the cyclotron frequency. In this limit, the scattering phenomena occur well before the electron can complete a cyclotron orbit around the atom, making quantum effects negligible [47].

In this frame, one can write the equation of motion for the electron:

$$\vec{F} = e(\vec{E} + \vec{v} \times \vec{B}) = m^*\dot{v} + \frac{m^*v}{\tau} \tag{3.6}$$

by solving the equation and splitting it into x and y, one can obtain:

$$(J_x + iJ_y) = \left(\frac{ne^2\tau}{m^*}\right)\frac{(E_x + iE_y)}{1 + i\omega_c\tau} \tag{3.7}$$

Lastly, by separating the real and imaginary parts of J, one can write σ_{xx} and σ_{xy}.

$$\sigma_{xx} = \frac{ne^2\tau}{m^*}\left(\frac{1}{1 + (\omega_c\tau)^2}\right) \tag{3.8}$$

$$\sigma_{xy} = \frac{ne^2\tau}{m^*}\left(\frac{-\omega_c\tau}{1 + (\omega_c\tau)^2}\right) \tag{3.9}$$

It is also possible to rewrite those equations using the mobility spectrum approach, where $\mu B = \omega_c\tau$ [52]:

$$\sigma_{xx} = \int_{-\infty}^{+\infty} \frac{s(\mu)}{1 + \mu^2B^2}\,d\mu \tag{3.10}$$

$$\sigma_{xy} = \int_{-\infty}^{+\infty} \frac{\mu B s(\mu)}{1 + \mu^2B^2}\,d\mu \tag{3.11}$$

Where $s(\mu) = n_s(\mu)q\mu$ is called the mobility spectrum [4].The equations hold only under the hypothesis that $s(\mu)$ is independent of the magnetic field B.

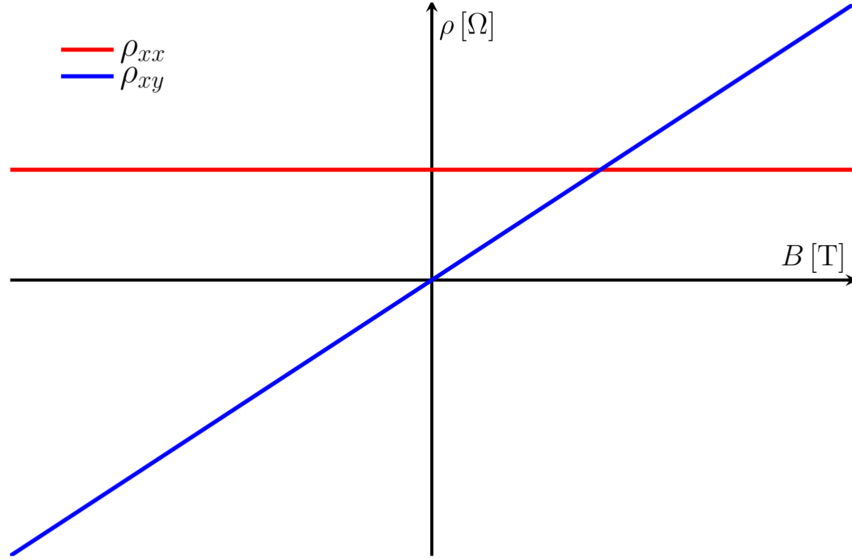

Figure 3.1: Qualitative behavior of ρ_{xx} and ρ_{xy} when a single carrier is present.

It is useful to define the Hall coefficient R_H, which can be expressed as:

$$R_H = \frac{E_y}{J_x B_z} = \frac{1}{ne} \tag{3.12}$$

This quantity describes the magnetic response of σ_{xy} to an external B. It also depends only on n, so it can provide information about the type of carriers you have inside the system (holes if $R_H < 0$, electrons if $R_H > 0$).

Also, at very low fields, you can link μ with R_H thanks to a simple equation:

$$\mu = \mu_H = \frac{R_H}{\rho_{xx}} = \frac{1}{n_H e \rho_{xx}} \tag{3.13}$$

μ_H and n_H are the Hall mobility and Hall density, respectively, and they are experimental estimates of μ and n.

It is also useful to consider the mobility spectrum approach for a moment. Due to the shape of $s(\mu)$, one can describe conduction driven by different carriers with different mobilities and densities. For example, a spectrum like this:

$$s(\mu) = n_0 e \mu_0 \cdot \delta(\mu - \mu_0) \tag{3.14}$$

describes the conduction driven by a single carrier with mobility μ_0 and density n_0.

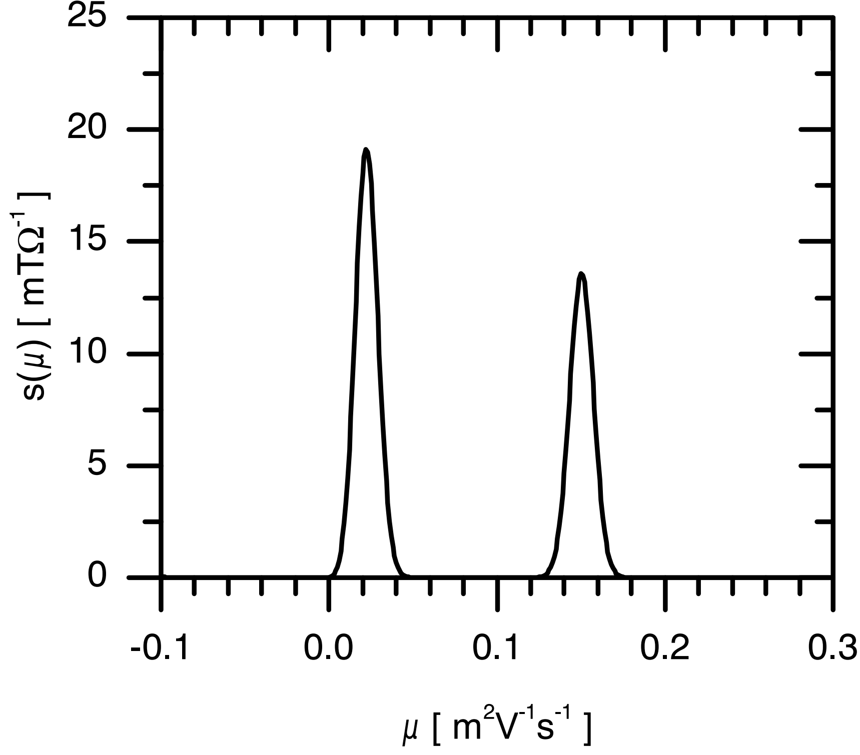

Figure 3.2: Mobility spectra calculated on synthetic data featuring two carrier gases of low mobility (Adapted) [4].

3.3. Two Carrier Model

Another interesting case to examine is the presence of 2 carriers, i.e. both electrons and holes in a conductor. This is typical of a surface channel in a device, or some GaN heterojunctions [53]. One can write the mobility spectrum of the system:

$$s(\mu) = n_A e \mu_A \delta(\mu - \mu_A) + n_B e \mu_B \delta(\mu - \mu_B) \tag{3.15}$$

Thanks to the (3.10) and the (3.11), the conductance terms can be obtained:

$$\sigma_{xx} = \frac{n_A e \mu_A}{1 + (\mu_A B)^2} + \frac{n_B e \mu_B}{1 + (\mu_A B)^2} \tag{3.16}$$

$$\sigma_{xy} = \frac{n_A e \mu_A^2 B}{1 + (\mu_A B)^2} + \frac{n_B e \mu_B^2 B}{1 + (\mu_A B)^2} \tag{3.17}$$

In this scenario, R_H depends on B. After some calculations, it can be written as:

$$R_H = \frac{\pm n_A \mu_A^2 \pm n_B \mu_B^2}{q(n_A \mu_A + n_B \mu_B)^2} \tag{3.18}$$

It is worth noting that the (3.18) is a general result and is also valid in a strong-field scenario. Moreover, if μB is large enough, the equation for R_H can be further simplified to the form:

$$R_H = \frac{1}{q(\pm n_A \pm n_B)} \tag{3.19}$$

showing how, if $\mu B \gg 1$, then R_H does not depend on μ at all, but only on the densities n_A and n_B of the carriers, similarly to the single carrier scenario discussed in the section 3.2.

3.4. Scattering magnetoresistance

The discussion above considers R_H independent of the scattering mechanism, thus magnetoresistance. In reality, in both single-carrier and double-carrier systems, the scattering mechanism creates a magnetoresistance that must be considered in the calculations of R_H [54, 55].

Magnetoresistance can be the result of different phenomena [56, 57]. A good way to consider them all together is to examine the dependence of the scattering mechanism on the energy. In particular, it is useful to define a *scattering coefficient* r:

$$r = \frac{\langle \tau^2 \rangle}{\langle \tau \rangle^2} \tag{3.20}$$

Where τ is the average scattering time, and the average is taken over the energy. This quantity can be directly expressed in (3.12) in the low-field case, leading to the following.

$$R_H = \frac{r}{ne} \tag{3.21}$$

For the strong-field case, R_H does not depend on magnetoresistance, so there is no reason to include this quantity.

3.5. Quantum treatment

At very low temperatures and high magnetic fields, some physical phenomena that cannot be explained by classical mechanics start to appear. In fact, they have to be treated with a quantum approach, as they are macroscopic manifestations of the quantum behavior of the system. Some of those effects are still not completely clear from a theoretical point

of view, but they can represent a powerful probe for studying the underlying behavior of quantum well devices.

In order to analyze the quantum phenomena, we start from the Schrödinger equation for a free electron in a magnetic field [47]:

$$\left[\frac{(\vec{p}-e\vec{A})}{2m^*}\right]\Psi = E\Psi \tag{3.22}$$

To represent the magnetic field, a Landau Gauge approach can be taken, by considering the vector potential $\vec{A}$:

$$A_x = -By \tag{3.23}$$

$$A_y = 0 \tag{3.24}$$

$$A_z = 0 \tag{3.25}$$

By separating the variables [58], one can write a wavefunction of the form:

$$\Psi(x,y,z) = e^{ik_x x}e^{ik_z z}\phi(y) \tag{3.26}$$

One can substitute and get to:

$$\left[\frac{(\hbar k_x + eBy)}{2m^*} + \frac{p_y}{2m^*} + \frac{\hbar^2 k_z^2}{2m^*}\right]\phi(y) = E\phi(y) \tag{3.27}$$

This can be rewritten in the harmonic oscillator form:

$$\left[\frac{m^*\omega_c^2}{2}(y-y_0)^2 + \frac{p_y^2}{2m^*} + \frac{\hbar^2 k_z^2}{2m^*}\right]\phi(y) = E\phi(y) \tag{3.28}$$

Where:

$$y_0 = -\frac{\hbar k_x}{m\omega_c} \tag{3.29}$$

The solutions of the equation are called *Landau Levels*, in the form of:

$$E_\ell(k_z) = \frac{\hbar^2 k_z^2}{2m^*} + \hbar\omega_c\left(\ell + \frac{1}{2}\right) \tag{3.30}$$

and ℓ is called the *Landau level index*. An important property of this system is that it presents a degeneracy in the x direction. In particular, the energy does not depend on k_x, which means that all levels are degenerate at a single value of n_x. In addition, this

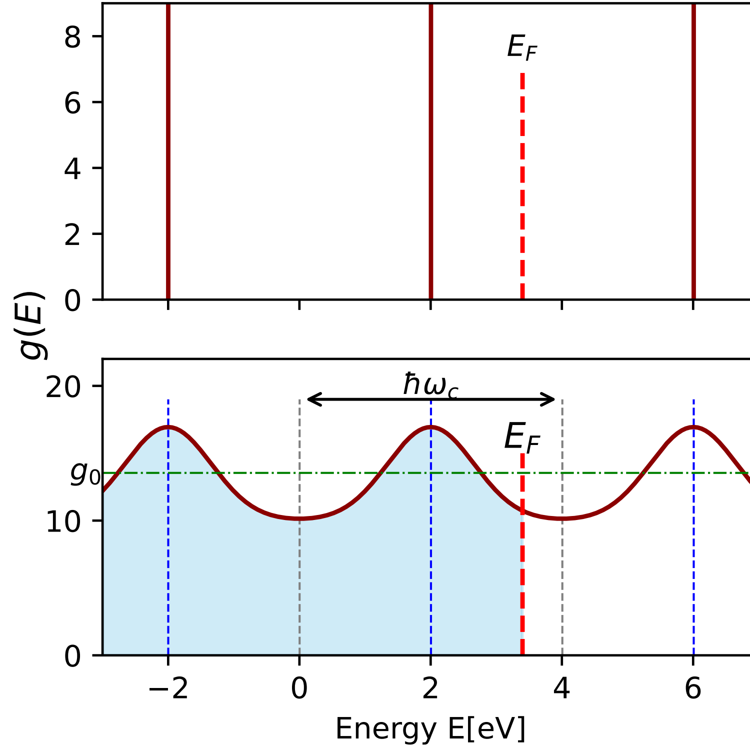

Figure 3.3: Simulation of the DOS function when an external magnetic field is applied. No broadening (top) or gaussian broadening (bottom) are considered.

degeneracy causes the density of states (DOS) to collapse into different δ-functions, called *Landau levels*.

y_0 has to lie within the sample, which has dimensions $L_x \times L_y$, so that:

$$-\frac{L_y}{2} < y_0 < \frac{L_y}{2} \tag{3.31}$$

Substituting y_0 leads to the following condition:

$$-\frac{m\omega_c L_y}{2\hbar} < k_x < \frac{m\omega_c L_y}{2\hbar} \tag{3.32}$$

Another important condition arises from the uncertainty principle, which forces k_y to have discrete values:

$$k = \frac{2\pi}{L_y} j \tag{3.33}$$

Where j is an integer which represents a degeneracy factor. One can combine both the

(3.32) and the (3.33) to obtain some constraint on j as well:

$$0 > j > \frac{eB}{h} L_x L_y \tag{3.34}$$

The allowed number of states per unit area becomes:

$$n_B = \frac{eB}{h} \tag{3.35}$$

Realistically, the δ-functions in the density of states $\rho_B(E)$ exhibit broadening due to both temperature and scattering mechanisms. In fact, the finite lifetime τ_q for the electron introduces a broadening of the energy E of $\hbar/\tau_q$ due to the Heisenberg principle (see Figure 3.3). The broadening can be considered either Gaussian or Lorentzian [59, 60].

It's also worth noting that if the broadening exceeds the Landau level spacing ($\hbar\omega < \hbar/\tau_q$), so if $\omega_c\tau_q < 1$, the Landau levels are not well resolved. As a consequence of that, in order to describe quantum phenomena, it is necessary to consider $\omega_c\tau_q > 1$.

Lastly, by changing the magnetic field, the spacing and n_B also change. The number of occupied Landau levels is called *filling factor* ν and can be written as:

$$\nu = \frac{n_{2D}}{n_B} = \frac{hn_{2D}}{eB} \tag{3.36}$$

Where n_{2D} is kept constant by moving E_F. This detail is quite important because, as B is changed, E_F will move between Landau levels proportionally to the $\rho_B(E)$ in that particular region. This also means that there are very small intervals of values for B to have E_F in-between Landau levels. The position of E_F plays a significant role in the Quantum Hall Effect phenomena.

3.6. Weak localization

Another interesting effect at very low fields is the weak localization effect. Due to quantum dephasing between weak and strong localization terms [61], longitudinal conduction σ_{xx} gains a negative correction term.

$$\Delta\sigma_{xx}(B) = \frac{e^2}{\pi h}\left[\Psi\left(\frac{1}{2} + \frac{\tau_B}{2\tau_\phi}\right) - \Psi\left(\frac{1}{2} + \frac{\tau_B}{2\tau}\right) + \ln\left(\frac{\tau_\phi}{\tau}\right)\right] \tag{3.37}$$

Where Ψ is the digamma function, τ_ϕ is the phase breaking time of the wavefunction, and $\tau_B = \hbar/2eDB$ with $D = v_F^2\tau/2$ as the diffusion constant. This behavior can be observed in Figure 3.4, where at very low fields, the magnetoresistance has a peak in zero, while it drops with increasing magnetic field by just a small amount.

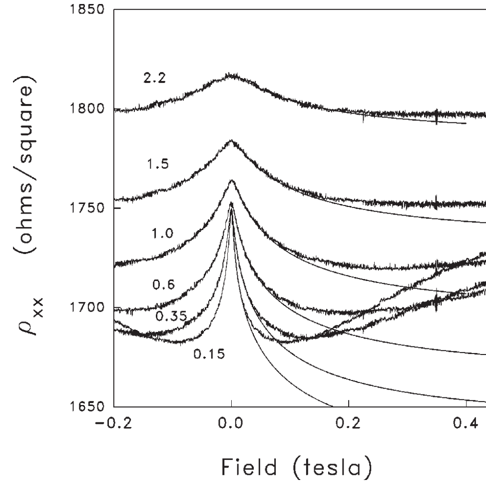

Figure 3.4: Weak localization regime. One can see the sudden decrease as the magnetic field moves from 0.

3.7. Shubnikov-De Haas Effect

The oscillatory behavior of the $\rho_B(E)$ is reflected in many different observables. One of them is the parallel resistivity ρ_{xx}, which presents growing oscillations as the field gets stronger. One can introduce the $\Delta\rho$ quantity as:

$$\Delta\rho = \frac{\rho_{xx} - \rho_0}{\rho_0} \tag{3.38}$$

Where ρ_0 is the longitudinal resistivity ρ_{xx} measured at zero magnetic field. Describing the SdH phenomenon in terms of $\Delta\rho$ is useful as it can isolate the oscillations from any other contribution, i.e. other magnetoresistance effects [62]. The equation describing the oscillations of $\Delta\rho$ is the Lifshitz-Kosevich equation [63, 64]:

$$\Delta\rho = 4\sum_{s=1}^{\infty} \frac{s\xi}{\sinh s\xi} \cdot \exp\left(-\frac{\pi\alpha s}{\mu B}\right) \cdot \cos\left(\frac{\pi h s n_s}{eB} - s\pi\right) \tag{3.39}$$

Where α is the Dingle ratio, n_s is the sheet density and ξ is defined as:

$$\xi = \frac{2\pi^2 m^* k_B T}{e\hbar B} \tag{3.40}$$

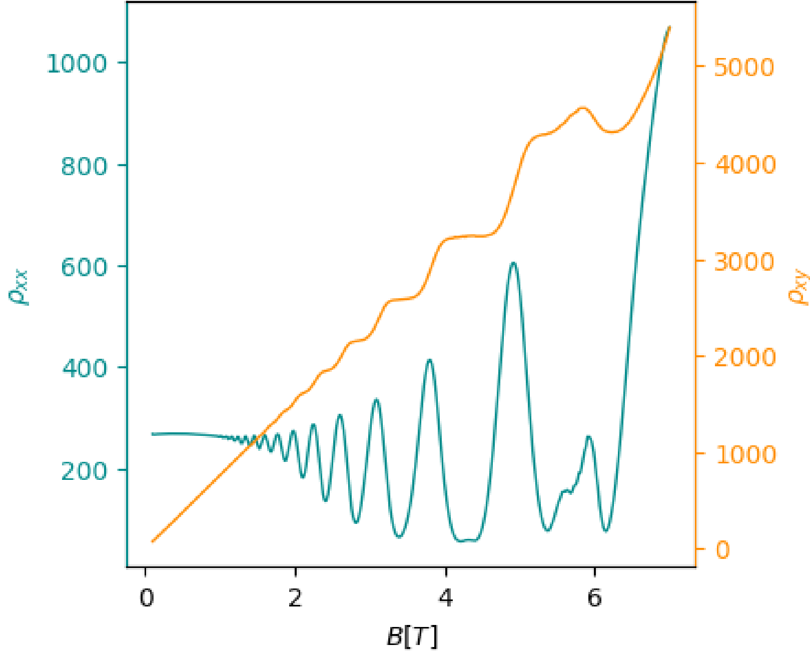

Figure 3.5: SdH oscillations and QHE measured on a similar HMOS respect to the structures analyzed in this work. Adapted from [5].

As the oscillations become stronger while the magnetic field is increased, there are values of B where ρ_{xx} reach zero, corresponding to a minima of the oscillations. This phenomenon can be explained by the fermi level E_F crossing the energies between the Landau levels.

Thanks to a fitting of (3.39), one can retrieve the values for the effective mass m^* and dingle ratio α. The methods will be analyzed in subsection 4.6.1.

3.8. Quantum Hall Effect

Another observable that is affected by the formation of Landau levels is ρ_{xy}. At high fields, there are broad plateaus at corresponding integer values of ν when E_F is between Landau levels and ρ_{xx} reaches zero. This effect is called the Quantum Hall Effect (QHE). In order to deeply understand this phenomenon, it is convenient to talk about carriers in a narrow channel. Starting again from the harmonic oscillator equation (3.28), and adding a potential $V(y)$ to take into account the walls of the channel [47]:

$$\left[\frac{m^*\omega_c^2}{2}(y-y_0)^2+\frac{p_y^2}{2m^*}+\frac{\hbar^2k_z^2}{2m^*}+V(y)\right]\phi(y)=E\phi(y) \tag{3.41}$$

Depending on the value of B, the energy of the states can change. However, in (3.41), the

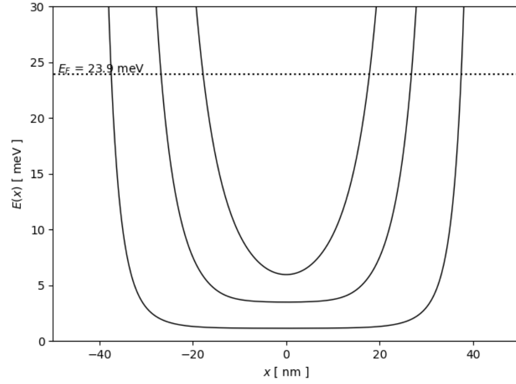

(a) Energetic levels of Edge States. One can observe how those states can move only in the regions very close to the edge.

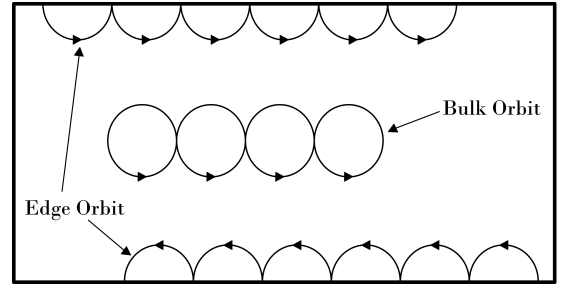

(b) Edge states representation. The name comes from the unfinished orbits near the edges.

carriers are affected by both B and $V(y)$, and depending on the shape of $V(y)$, one can be dominant over the other. Generally, in a channel, one can expect that the electrons in the middle are less affected by $V(y)$ and are squeezed to very low energies by B, while the carriers on the edge are highly affected by $V(y)$ and can have energies close to E_F. These high-energy electrons on the side of the channel are called *edge states* and are the only available carriers in a strong-field regime.

The behavior of edge states can be understood by considering the cyclotron orbits in the sample. Generally, those circular orbits are completed, so the net drift velocity of the particle is zero. However, near the edges, those orbits are interrupted by the walls, which means the carriers acquire a drift velocity $v_d \neq 0$. The result is a *skipping orbit* that bounces along the boundary of the channel (Figure 3.6b). This mechanism leads to an important property for those carriers: the states on opposite edges travel in opposite directions.

Another characteristic of edge carriers is that they can suppress scattering due to the broken time reversal symmetry caused by the presence of B [65]. So, at very high magnetic fields, the carriers near the center of the channel lose the ability to conduct, and conduction is driven only by the edge states, which provides zero-resistance conduction.

3.8.1. Fractional Quantum Hall Effect

In the extreme conditions of high field and low temperature that make QHE observable, all the carriers remain in the lowest Landau level and spin states. However, at even higher fields and lower temperatures, there is the possibility that all the carriers in the lowest level create an order under the influence of their mutual interaction. In this condition, some electron states have been found to have fractional occupation ν of the lowest Landau level

[66, 67]. This phenomenon is referred to as the Fractional Quantum Hall Effect (FQHE).

For this effect to arise, very high mobility samples are needed in order to enhance electron-electron interactions over the electron-impurity ones. It's worth noting that in FQHE, plateaus appear for defined values of ν, i.e. $1/3, 2/3, 3/5, 5/7$. Recently, even denominators for ν have also been observed in GaAs samples [68]. Lastly, FQHE states have been predicted to carry fractional charge, i.e. $e/3$ for $\nu = 1/3$. This effect is strange on its own, and the debate about the properties of the phenomenon is still very active.

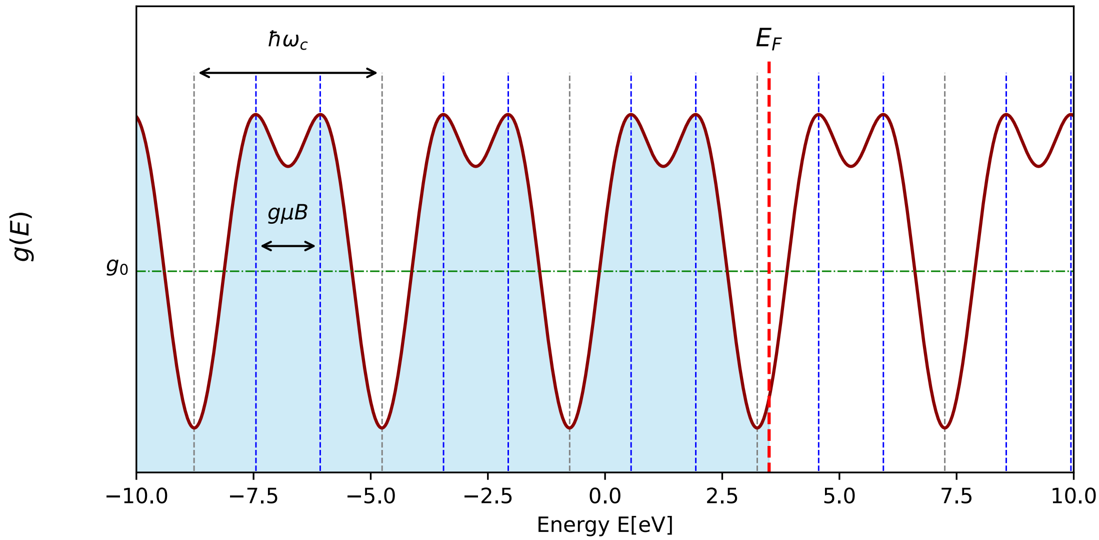

Figure 3.7: Simulation of the DOS function at high magnetic field ($B = 5T$).

3.9. Spin splitting

Another important effect to take into account is the spin splitting of the Landau levels. As a magnetic field is present, electrons with different spins will have a contribution in energy related to their spin, according to the Zeeman energy splitting [69]. Adding this energy to the (3.42) leads to:

$$E_\ell = \hbar\omega_c \left(\ell + \frac{1}{2}\right) \pm \frac{1}{2} g\mu_B B \tag{3.42}$$

Where $k_z = 0$ for simplicity. In the (3.42), the g-factor is equal to 2, and μ_B is the Bohr magneton:

$$\mu_B = \frac{e\hbar}{2m_0} \tag{3.43}$$

The Zeeman splitting of the Landau levels doubles the peaks in the shape of $\rho_B(E)$

(Figure 3.7). This splitting is then visible in all phenomena involving the oscillation of the DOS, i.e. SdH oscillations and QHE plateaus. It's worth noting that the effective value of g can be written as [70]:

$$g^* = \frac{2m_e}{m^*} \frac{1}{1 + \sqrt{B_S/B_L}} \tag{3.44}$$

Where B_S and B_L are, respectively, the fields at which the splitting occurs and the field at which the oscillation begins.

4 | Experimental Techniques

4.1. LEPECVD

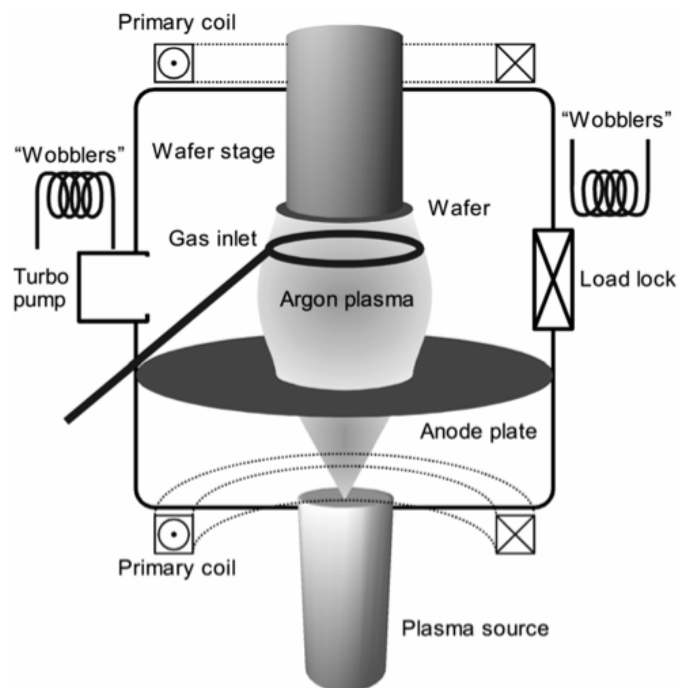

Figure 4.1: LEPECVD reactor setup scheme.

Low-Energy Plasma-Enhanced Chemical Vapor Deposition (LEPECVD) is a deposition technique used to epitaxially grow all of the devices analyzed in this thesis. The working principle is similar to a standard CVD technique, with a fundamental difference in the reaction driving mechanism [33, 71, 72, 73]. The main difference is the presence of a low energy, high density DC argon plasma focused onto the Si wafer. The plasma cracks the gasses present in the chamber, generating highly reactive radicals that are then deposited onto the wafer. Moreover, the hydrogen released by the reactant gases can passivate the surface: This passivation layer is removed by inducing the ion bombardment onto the surface. Is important to note that the energy of the ions is very low, i.e. 10 eV, in order not to damage the crystal.

The reaction chamber is kept in Ultra-High Vacuum (UHV) conditions: while idle the base pressure is on the order of 10^{-9} mbar. The role of UHV is very important as it decreases the levels of contaminants and improves the control of deposition in the chamber. During a deposition process Ar and process gasses bring the pressure to 10^{-2} mbar.
The precursors used for deposition are SiH_4 and GeH_4 for SiGe layers, while PH_3 and B_2H_6 are used to introduce the n and p dopants, respectively.
A heating stage made of pyrolitic graphite cladded between boron nitride disks is used to bring the substrate to the temperatures required for high crystal quality. Temperature plays a significant role in the deposition rate (DR). In a classical CVD technique, there is an exponential dependency between the two quantities such that a very high temperature is needed to achieve acceptable deposition rates. Furthermore, Ge and Si have different H desorption rates, so there is a very high temperature dependence on the SiGe DR. However, in the case of LEPECVD, the DR value is mostly controlled by plasma energy and density, in a range from < 0.1 nm/s to 10 nm/s. making the technique more flexible and allowing for wider ranges of operating temperatures.

4.2. Samples

Different HMOS have been grown using LEPECVD, with different Ge QW thicknesses. The stack is represented in Figure 4.2.

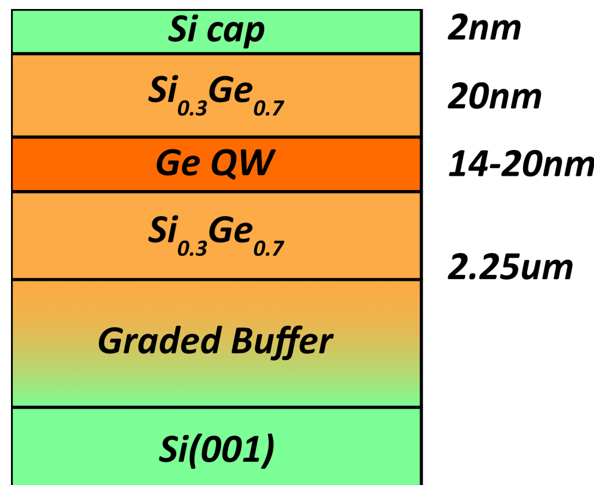

Figure 4.2: Stack of the HMOS samples analyzed in this work.

Then, Hall bars were fabricated from this stack in order to characterize the sample. More details are described in section 4.4.

Along with HMOS, some Ge channels have also been characterized thanks to a Hall bar

structure. These Hall bars have been fabricated by IST Austria and sent to L-NESS for characterization in order to study how conduction changes in the case of high strain when Ge is grown at very low temperatures (200-300°C). This temperature range is compatible with the typical values of the back end of the line (BEOL) processes, decreasing the overall thermal budget needed for growing the structure. The stack is represented in Figure 4.3.

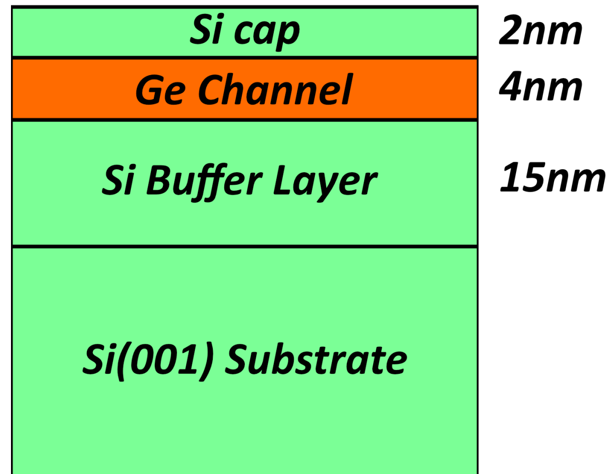

Figure 4.3: Stack of the highly strained Ge channel analyzed in this work.

4.3. Hall bars

In order to characterize the substrates grown using LEPECVD, the fabrication of Hall bars is necessary. A Hall bar is a cross-shaped structure with six different contacts, such as the one represented in Figure 4.4. The middle region is called the *body*, and the current can flow between its contacts. During this process, a voltage can be measured between the other four contacts (the *leg* contacts), which are laterally connected to the body. In this way, one can measure both the longitudinal voltage V_{xx} and the transversal voltage V_{xy}. Then, utilizing the current flowing through the channel, one can obtain a very accurate measurement of the resistances and thus the resistivity ρ_{xx} and ρ_{xy}. Moreover, the Hall bar can also be gated, depositing an oxide/metal stack on the body to apply a gate voltage on the channel.

4.4. Fabrication

Fabrication of Hall bars has been done for HMOS samples in the L-NESS and Polifab cleanrooms, involving different procedures. Strained Ge Hall bars were created at ISTA instead, utilizing a very similar process flow.

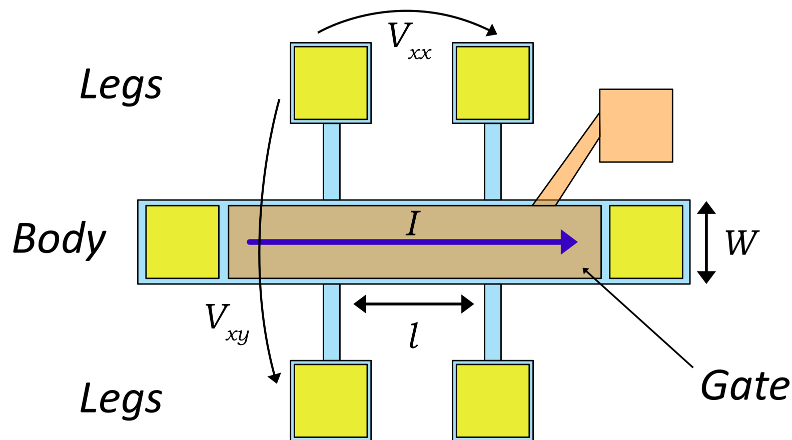

Figure 4.4: Hall bar representation. One can observe both the body and legs of the bar, as well as the w and l values from which the geometrical ratio is obtained.

The substrate was cut into 1×1 cm^2 squares. The process consists of four different fabrication steps. In order:

- Patterning of metallic contacts
- Definition of the Hall Bar mesa
- Deposition of the gate oxide
- Deposition of the metallic gate

The fabrication steps are represented in Figure 4.7. Each major step will be treated separately.

A lithographic mask has been prepared according to the fabrication steps, in order to define the geometry and structure of the Hall bar. A more linear and simple design has been chosen (Figure 4.5) with respect to ISTA devices, as the work focused on establishing a baseline in the fabrication process. The characterization of this first generation of devices will bring about an optimization of the whole design and process in the future iterations.

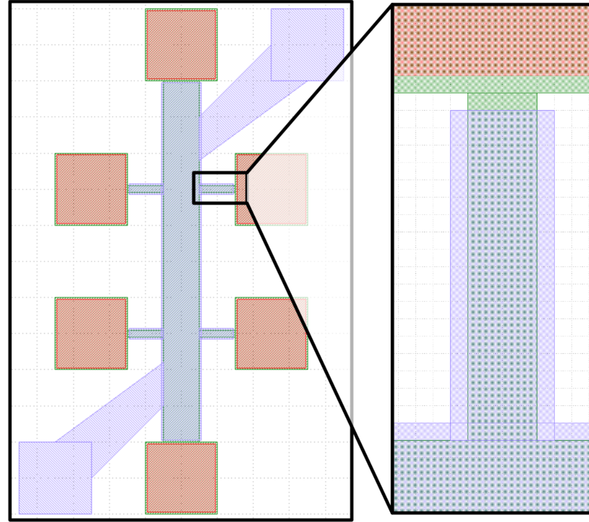

Figure 4.5: CAD drawn litographic mask for a gated Hall bar designed for this work. One can see the close-up to a leg of the Hall bar, revealing a region where no gate has been deposited to avoid overlap with the contact pad.

Then, two different masks have been prepared. In the first, two scaled versions of the Hall bars have been added, with scaling factors of 80% and 120%, respectively. In the second mask, the Hall bars have been rotated by 22.5°, 45°, and 67.5°. These two can be visualized in the Figure 4.6 The objective was to create hall bars with different dimensions and orientations and to characterize transport properties concerning both device-related effects and the effective mass anisotropy effect (see section 1.4).

4.4.1. Patterning of metallic contacts

The sample was chemically cleaned with acetone and isopropyl alcohol and prepared for a lithographic process. On top of the sample, a layer of Ti-based primer is spin coated at 6000 rpm to improve the adhesion and uniformity of the photoresist. The primer is then baked to 120°C, to make the solvent in the primer evaporate. A negative photoresist (AZ15nXT) is then spin coated at 4000 rpm and another heating process is performed at 110°C.

The mechanism behind an optical lithography step is based on the photo-reactions inside the resist. In the case of a negative resist, those reactions strengthen the cross-linking between chains of the resist, making it less soluble and ready for a development step. Furthermore, AZ15XT is a Chemically Amplified Resist (CAR) and contains a PhotoAcid Generator (PAG). This makes all the baking steps crucial, as they activate the PAG molecules and amplify the cross-linking.

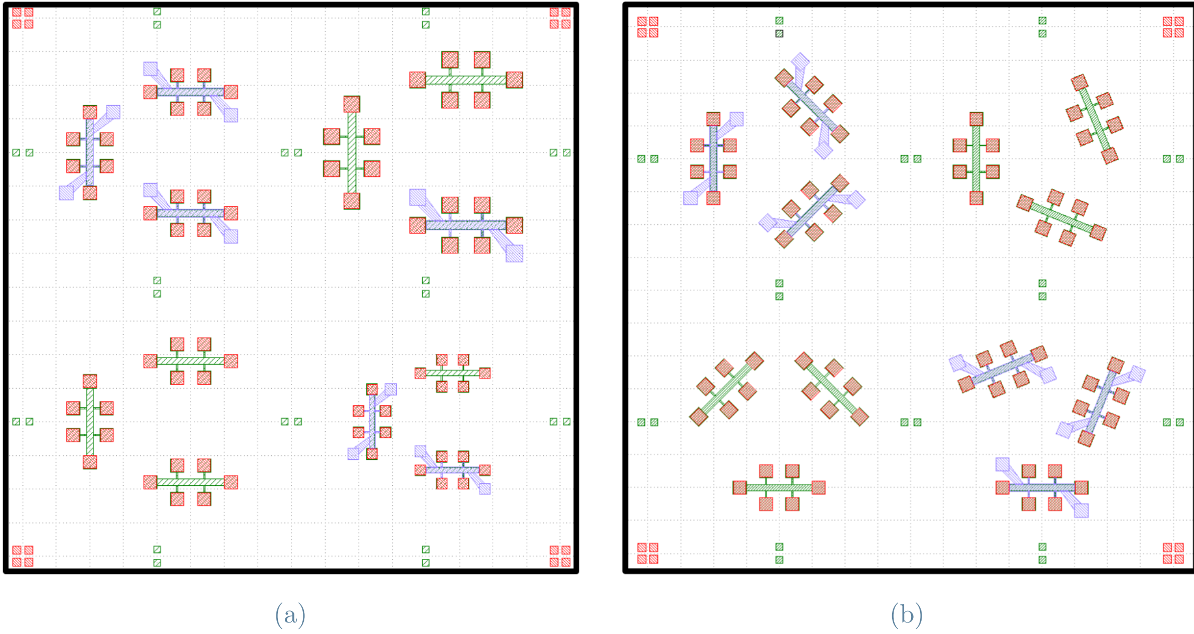

(a) (b)

Figure 4.6: Final lithographic masks used on the samples. Hall bars have been (a) scaled and (b) rotated respectively.

A Heidelberg MLA100 is used to print the design on the sample. With 365 nm light and a set dose of 350 mJ/mm^2, the Hall bar contact regions have been imprinted with light in the resist. In order to reveal them, a Post-Exposure Bake (PEB) at 120°C for 60 s makes cross-linking possible. Lastly, immersion in AZ 726 MIF is performed for 120 s. This dissolves the most soluble parts of the resist, creating the actual pattern onto the sample.

Lithography is performed multiple times in the process flow, using similar parameters and procedures.

To deposit contacts, a first cleaning in HF diluted to 5% was performed to remove any native oxide layer from the surface. Then a Leybold L560E was used to deposit 10 nm Ti and 150 nm Au, which will form the contacts. The Ti layer is deposited as an adhesion layer between the gold and Si without changing the electrical properties of the device. The evaporator utilizes a very high-energy electron beam focused on a crucible containing solid metal which evaporates due to the beam. The sample is positioned $\tilde{3}0$ cm away from the crucible, with the patterned side facing the crucible.

Lastly, a lift-off is performed by submerging the samples in NI555 remover to dissolve the resist, which is then washed away with excess gold using isopropanol.

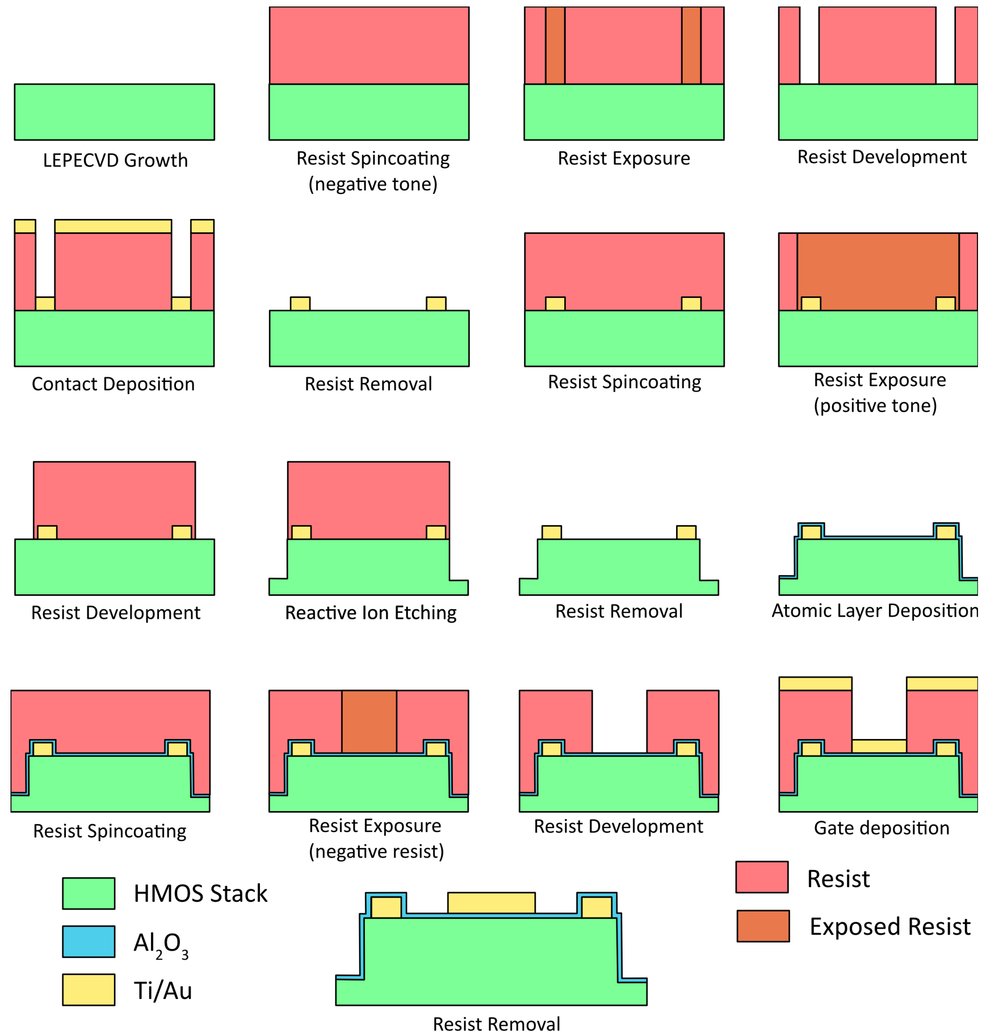

Figure 4.7: Hall bar fabrication process flow. The representation shows a cross-section of the device, taken at the leg point of the Hall bar.

4.4.2. Definition of the Hall bars

Another lithography is performed to cover the contacts with resist. This is done with a positive resist (AZ12XT) rather than a negative one.The reason comes from the profile of the resist after development, as sketched in Figure 4.8. Generally, positive resists are preferred for etching purposes, while negative ones are better for depositions. This is due to different factors, the most important one being the etch resistance. In fact, thanks to the cross-linking induced by light, negative tone resists have much higher etch resistance, making them more reliable in a etching process and more resistant to pattern collapsing.

The next step is to etch away material around the Hall bars in order to isolate the QW structure. This is done using the Reactive Ion Etching (RIE) technique, which utilizes chemicals in a plasma to etch the surface both physically and chemically. The sample

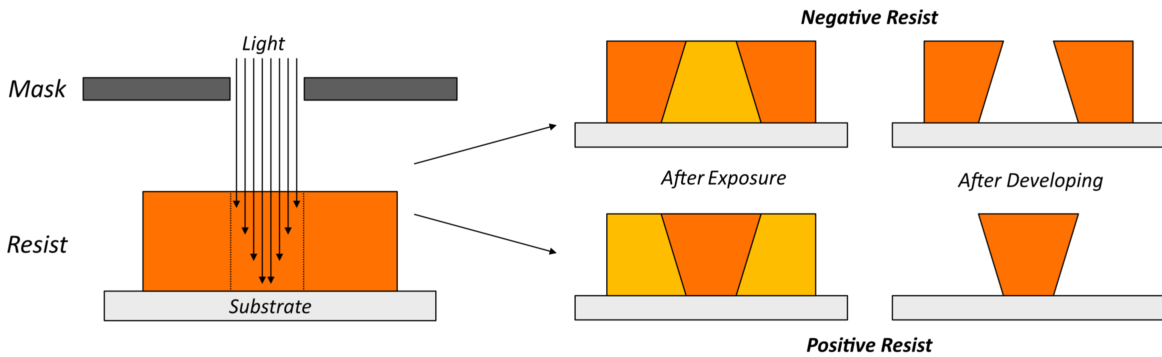

Figure 4.8: Different resist profiles depending on resist type.

is glued to a loading wafer to achieve stable thermal conduction and inserted into the chamber of an SPTS Omega Synapse 200 LPX. A Bosch recipe is used, which alternates plasma etching steps with SF_6 and polymer passivation with C_4F_8. This cycle is repeated 24 times in the chamber to etch 260 nm of material, and the result of the process is shown in Figure 4.10. The actual etching depth that has been reached is much lower, around 120 nm. The resist was then removed using P1331 heated at 70°C as a stripper.

4.4.3. Deposition of the oxide

A 20 nm nominally thick layer of Al_2O_3 has been deposited onto the entire surface with a Beneq TFS 200, an Atomic Layer Deposition (ALD) tool. The ALD is a vapor deposition technique in which a precursor and a reactant are released in the chamber in an alternating sequence. Thanks to this procedure, the growth can be controlled layer-by-layer, achieving maximum uniformity and control. Similarly to CVD techniques, ALD can also be improved by using a remote plasma source. The radicals emitted by the plasma enhance the reaction, lowering the required temperature for a target DR. Generally, the thermal-mode and the plasma-mode produce similar results, with very slight differences in the conformality of the film.

In order to test extensively the ALD process, both plasma-ALD and thermal-ALD have been utilized on different samples, at 90°C and 200°C, respectively. No mask was prepared for this deposition and the oxide layer was deposited onto the whole sample, including the gold contacts. This choice was suggested directly by the ISTA Hall bar fabrication process, and it is based on the idea that the soldering process needed to electrically bond the devices on the chip carriers will break the oxide and form a low-resistance ohmic contact. A further step of the activity, beyond the scope of this work, will refer to the development of both lift-off and etching recipes for Al2O3, increasing flexibility in the

process design.

Characterizations were performed on the deposited oxide: a control Ge-on-Si sample was inserted into the chamber together with the device samples in order to later measure the film thickness by ellipsometry. Ellipsometry measures the change in the polarization of light as it is reflected or transmitted through a medium. By setting an incident angle and then projecting monochromatic light onto the sample, the transmitted amplitude ratio $\Psi(\lambda)$ and the phase difference $\Delta(\lambda)$ can be measured. These quantities show a dependence on thickness and optical constants. Then, by extracting these values for different wavelengths, one can obtain useful information on the multilayer. In this case, the thickness of the film has been extracted from the fitting in Figure 4.9, which corresponds to 20.5 nm.

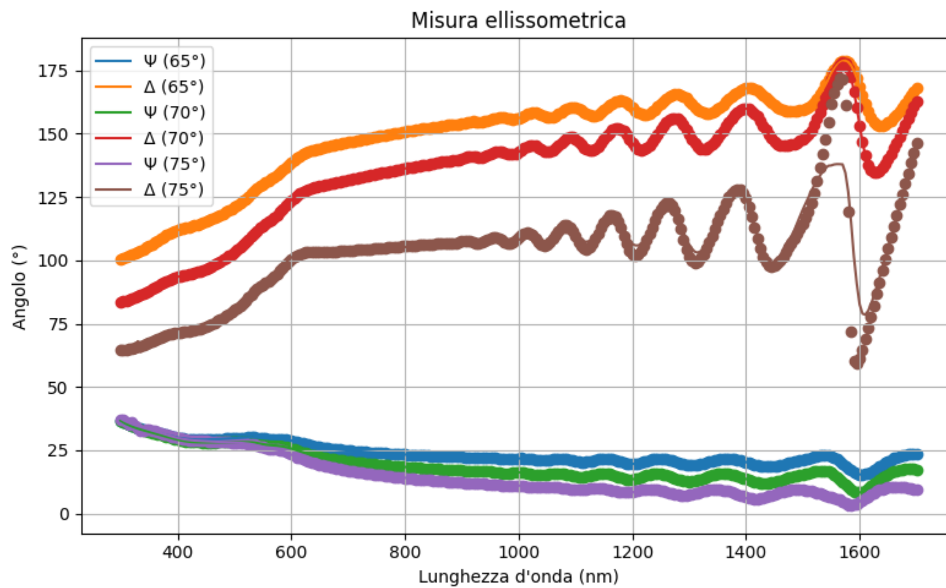

Figure 4.9: Oxide spectra taken thanks to a J.A. Woollam VASE Ellipsometer. The spectra were fitted according to a multilayer model using the tabulated optical constants of Si, Ge and Al_2O_3 while leaving the thickness of the layers as free parameters.

One of the complete devices has also been cleaved, producing an indentation in the wafer to crack it along the crystalline directions. In this way, a Hall bar has been broken in half to take images of the cross-section of the device, thanks to a Scanning Electron Microscope (SEM). Figure 4.10 clearly shows the presence of the oxide layer, and its thickness appears to be on the order of 20 nm.

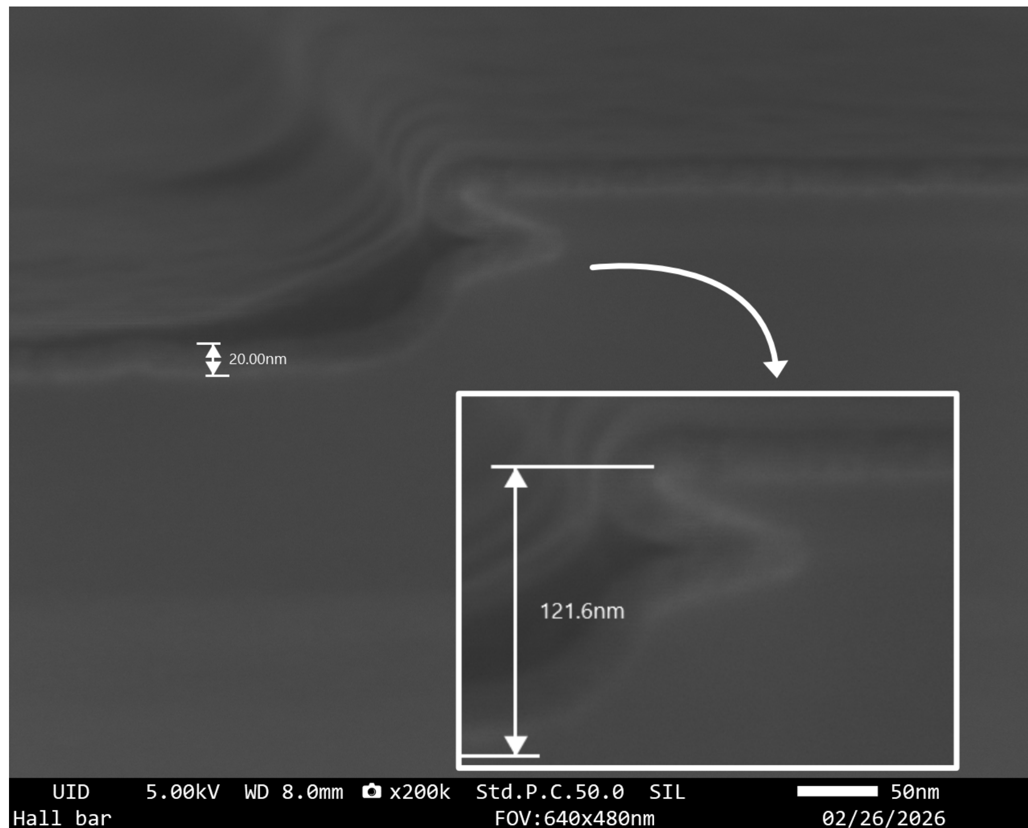

Figure 4.10: SEM image taken on the edge of the Hall bar pad. One can see the etching profile, as well as the oxide adhesion to the stack. The layer appears to be perfectly conform to the HMOS, even on the vertical wall formed by the etching step. A zoom on the wall is shown to see the etching profile created. Out of the 260 nm target depth, only 120 nm have been etched. Furthermore, the Ge QW has been laterally etched more than the corresponding $Si_{0.3}Ge_{0.7}$ layer, creating an indentation in the wall profile.

4.4.4. Deposition of the gate and finishing steps

The deposition of the gate is similar to that of the contacts. Firstly, a lithographic process is performed to define the area of deposition. Then a 10 nm Ti layer and a 150 nm Au layer are deposited. Lastly, a lift-off is performed to remove excess gold.

The metal was not deposited onto all samples: some of them were left without a gate. It is known that different fabrication processes and machines tend to trap a higher or lower number of charges in the oxide. These charges can activate the QW channel even at low temperatures, where no conduction should be possible because of the freeze-out regime. To understand whether the grown oxide contains charges or not, some devices were left without the gate and tested at low temperatures to check whether conduction was possible.

The samples were then cleaved and divided into smaller pieces. They were glued to a chip

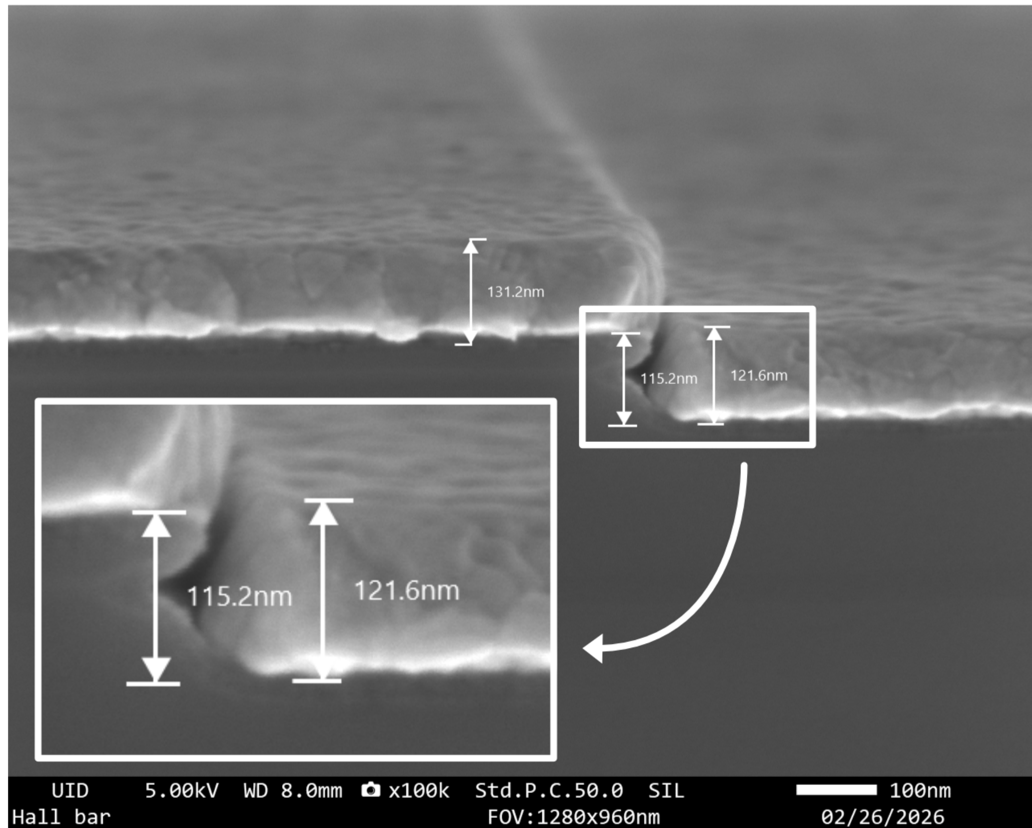

Figure 4.11: SEM image taken on the body of the Hall bar. One can see both the gold and the oxide layers, as well as the etching profile. From the image, it is really hard to predict the thickness of the oxide layer in this region.

carrier with silver paste to achieve good thermal contact with the holder, and then the contacts were bonded to the holder. In this way, the samples were ready to be mounted on the cryostat head.

4.5. Cryostat

Different samples were measured with a cryostat (Cryogen Free Element System (CFES), from Cryogenic) at low temperatures and high magnetic fields. In order to achieve such extreme conditions, a superconductor coil has been used to reach 7.5 T to investigate the magneto-transport properties of the structures.

The cryostat can reach 1.6 K in temperature, and the temperature can be controlled in a range between 1.6 K and 300 K. This is achieved thanks to a helium loop that continuously pumps through the system between a tank, a refrigerator, and two different stages. The first stage is a high-temperature stage, around $T = 40$ K while operational. The role of this stage is to provide stability to the temperature of the cryostat, limit heat exchange,

and confine the high magnetic field. Inside, there is the second stage, which is smaller but can reach $T = 4$ K. This is where the holder with the sample will be positioned, as well as where the magnetic field will be generated.

Helium flow is crucial for the operation of the cryostat, as a lower amount increases the temperature, while a larger amount than necessary causes the helium to condense into the circuit, stopping the system from functioning. This is regulated by a needle valve positioned above the second stage and plays a key role in the functioning of the system.

It is also worth noting that lower temperatures have been reached as a result of a transient regime in the chamber. By accumulating liquid He in the tank and then opening the He valve, a stable 1.6 K temperature can be maintained for approximately 1 hour. This exploit has been used to measure the samples at temperatures even lower than 4 K in some scenarios.

4.6. Methods and analysis

4.6.1. ρ_{xx} and ρ_{xy} analysis

Different methods have been used to retrieve meaningful information and parameters about the HMOS structure. First, measurements of both ρ_{xx} and ρ_{xy} have been taken with respect to the magnetic field from -7.5 T to 7.5 T. These sweeps in the magnetic field have been conducted multiple times at different temperatures to obtain different curves with respect to both T and B. To obtain mobility and hole density, (3.13) was used, starting from the measurement of ρ_{xx} and ρ_{xy}.

The background has been removed from the oscillations using different techniques like the Savitzky-Golay method [62], interpolation, moving mean method, 2nd derivative. These have been tested on pre-measured data provided by an older Ge/SiGe HMOS study [5]. The goal was to understand which method would give the best results. The most promising ones came from the Savitzky-Golay and moving mean methods. In particular, the Savitzky-Golay method seems to be the most robust and can maintain a mean value of the curve very close to zero, as shown in Figure 4.12.

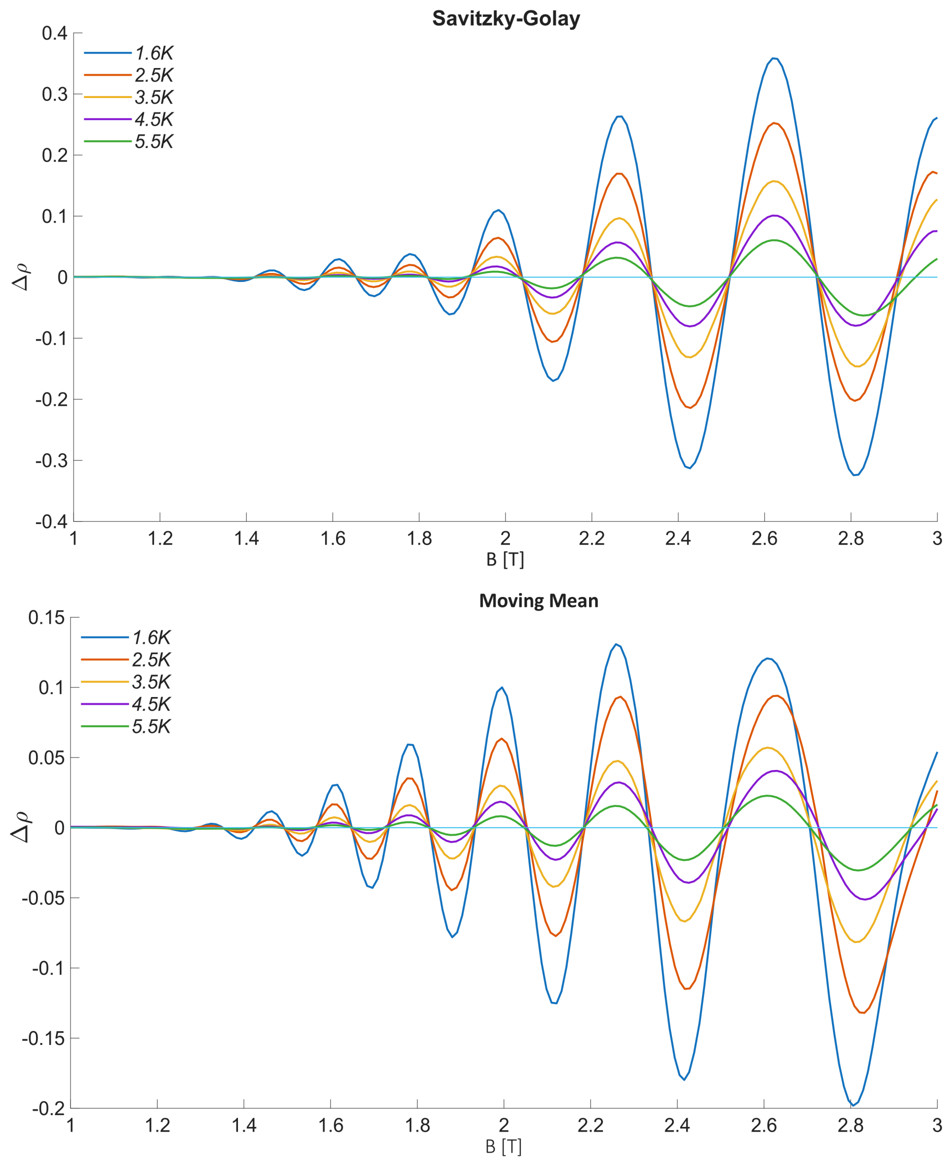

Figure 4.12: Comparison between extracted data with a Savitzky-Golay method and a moving mean method. One can see that the latter is way more instable and produces a result that globally has not a mean value of 0.

Then, the effective mass m^* has been obtained by analyzing the SdH oscillations, whose temperature dependence can be visualized in (3.39):

$$\xi = \frac{2\pi^2 m^* k_B T}{e\hbar B} \tag{3.40}$$

$$\frac{\Delta\rho_{xx}(T)}{\Delta\rho_{xx}(0)} = \frac{\xi(m^*)}{\sinh\left(\xi(m^*)\right)} \tag{4.1}$$

Taking the ratio between two points with the same B and different T, one can obtain:

$$\frac{\Delta\rho(T_1)}{\Delta\rho(T_2)} = \frac{\xi(T_1)}{\xi(T_2)} \frac{\sinh(\xi(T_2))}{\sinh(\xi(T_1))} \tag{4.2}$$

Then, one can solve (4.2) for m^*. This procedure has been applied between all adjacent points, and the values have been averaged to obtain an estimate of the value of m^*.

To obtain the dingle ratio α, (3.39) has been used again, this time by fixing the temperature to a maximum or minimum of the oscillations ρ_{xx} and utilizing the values m^* obtained previously:

$$\ln\left(\frac{\Delta\rho_{xx}}{\rho_0}\frac{\sinh(\xi)}{4\xi}\right) = -\frac{\pi\alpha}{\mu B} \tag{4.3}$$

By fitting the left term with respect to $1/B$, one can retrieve the slope and thus the value of α. The plot that represents all those points is commonly referred to as the *Dingle plot*.

4.6.2. FFT Analysis

Frequency analysis of SdH oscillations can be performed to obtain different information about the system. By calculating the Fast Fourier Transform (FFT) of the oscillations, one can retrieve the frequencies and amplitudes of all oscillating components. The oscillating term in the density of states is given by [44]:

$$\cos\left(\frac{2\pi s E_F}{\hbar\omega_c} - s\pi\right) \tag{4.4}$$

in which

$$E_F = \frac{\hbar^2 k_F^2}{2m^*} \tag{4.5}$$

and k_F is given by:

$$k_F^2 = 2\pi n_s \tag{4.6}$$

while ω_c is the cyclotron frequency

$$\omega_c = \frac{eB}{m^*} \tag{3.5}$$

This means that the oscillations are periodic in $1/B$, such that

$$n_s = \frac{e}{\pi\hbar\Delta(1/B)} \tag{4.7}$$

Therefore, by calculating the frequency of the peaks, one can retrieve the carrier density in the system. This has been compared with the value obtained with (3.12) for consistency.

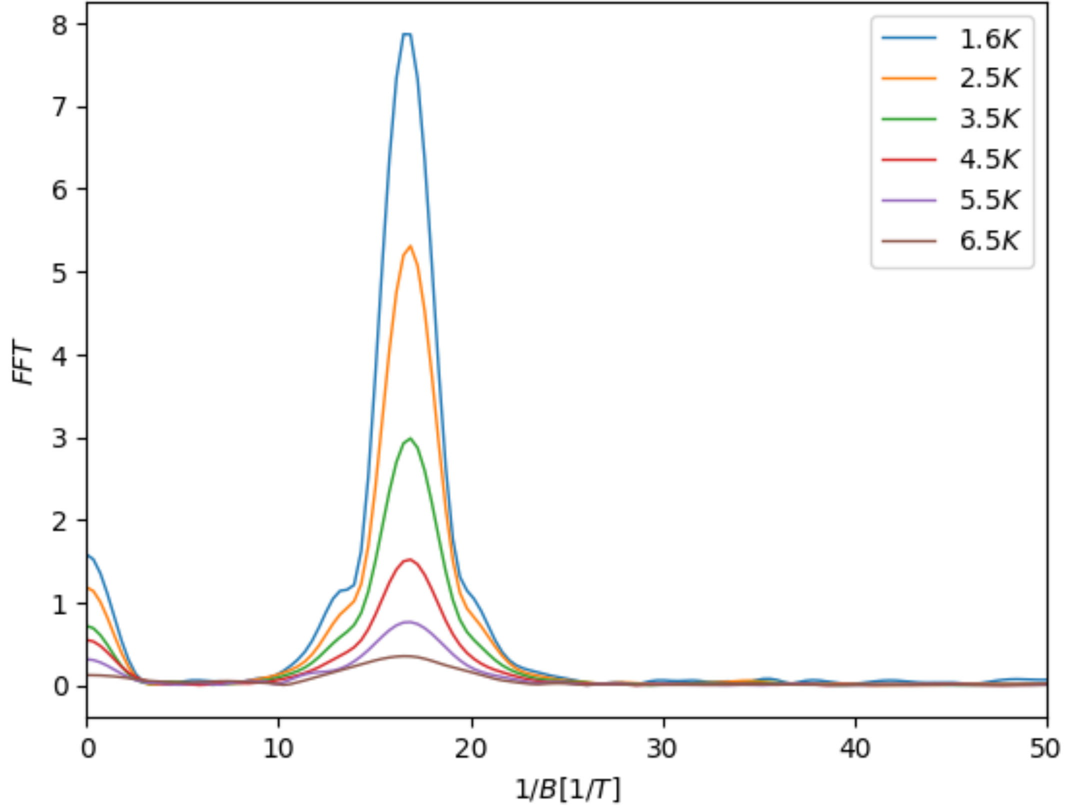

Figure 4.13: FFT analysis of the HMOS SdH oscillations at different temperatures. Extracted from the data represented in Figure 4.12.

4.6.3. Percolation density

A percolation density analysis was performed when possible. As described in section 1.3, a higher gate bias corresponds to a larger QW where carriers can accumulate, leading to better conduction. This mechanism can be studied in the 2D-MIT region (i.e. the threshold region) in order to characterize the percolation density of the device.

Measurements of Hall density n_H and mobility μ can be taken at different gate voltages V_g, creating a curve that describes the 2D-MIT behavior. Then, one can retrieve σ with respect to n_H by using:

$$\sigma = n_H q \mu_H \tag{4.8}$$

and fit the result in the (2.23):

$$\sigma = (n - n_p)^p \tag{2.23}$$

In this way, an estimate of n_p and p, can be obtained, and the latter can be confronted with a theoretical value of 1.31.

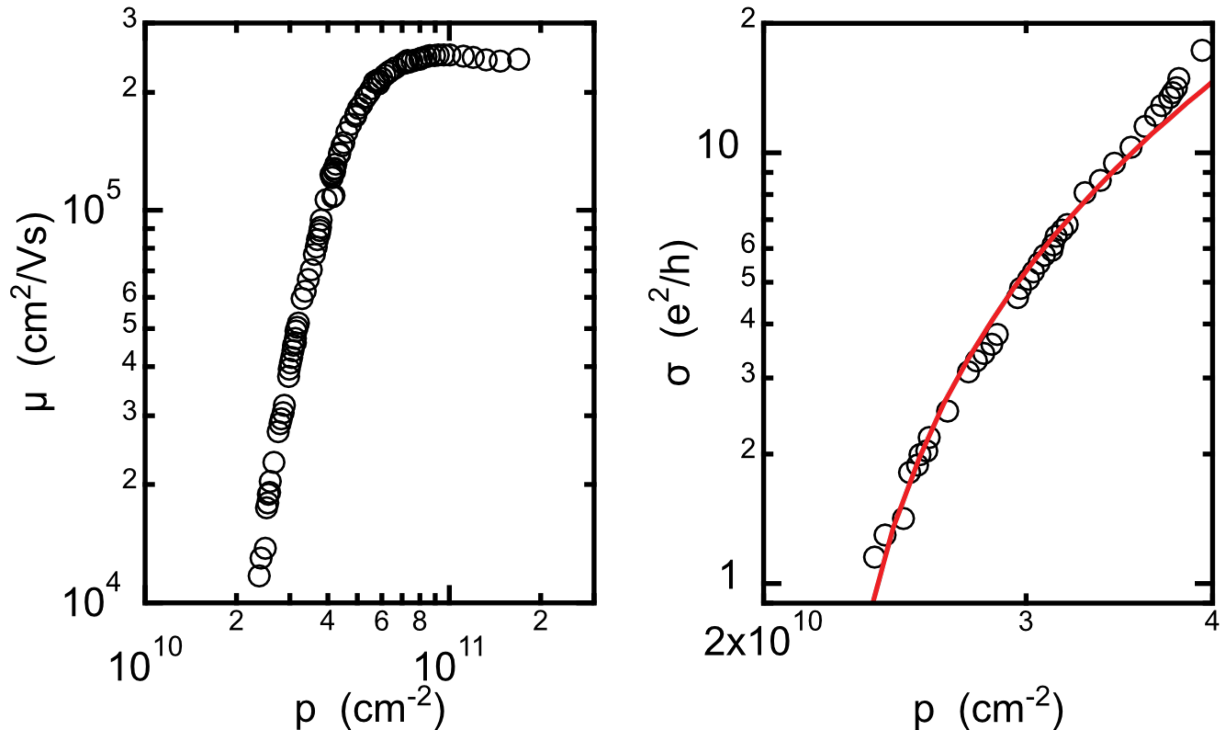

Figure 4.14: Example of a Ge/SiGe HMOS percolation density analysis [6]. Starting from the measurements of μ for different values of n_H taken by changing V_g (left), one can then calculate $\sigma(n_H)$ and plot the corresponding curve (right). The red line is the theoretical fit with the (2.23).

5 | Highly Strained Ge Samples Analysis

All fabricated samples were electrically characterized. To maintain a clear explanation of the analysis, the experimental data will be labeled with numbers (represented in Figure 5.1) that refer to the pads used for the measurement.

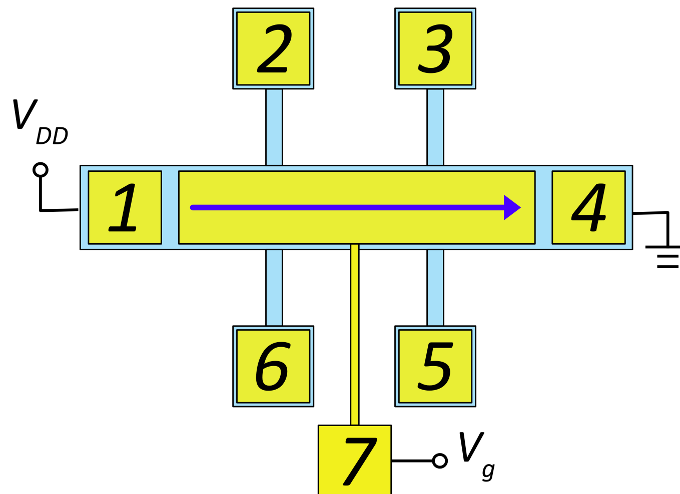

Figure 5.1: Schematic figures of a Hall bar, with enumerated contact pads and the current flowing from pads 1-4. The Hall bar analysis will always refer to these numbered contacts, with the 7th pad simply not present in the case of the oxide-no-gate Hall bars.

5.0.1. 11607 sample

The 11607 sample is characterized by a 4 nm Ge channel grown at 200°C, as indicated in Figure 5.2. Using this structure, Hall bars have been fabricated at ISTA with different designs. The freeze-out of the contacts has been a significant concern; therefore, three similar designs have been tested, with some small differences in the leg contact regions. Some optical images have been taken and are shown in Figure 5.3.

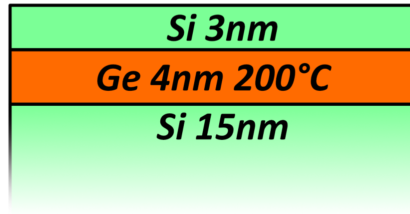

Figure 5.2: Stack of the 11607 channel region.

Another important parameter to consider is the intrinsic Ge conductivity. With no doping, the typical intrinsic Ge resistivity for such a small channel is in the order of $\rho \sim 10^5$ Ω·cm at room temperature. On top of this, the freeze-out at low temperatures makes the sample unable to conduct at all if no very high gate bias is applied. However, having a high bias at the gate can break the oxide dielectric, creating total leakage and permanently damaging the Hall bar.

The Hall bar testing proved the hypothesis. At room temperature, the conductivity of Ge was very low, with a resistivity greater than 80 kΩ. In addition, a leakage current has been found to flow from the contacts through the gate, with a resistance in the range of $\sim$ 100Ω. This suggests that the gate was shorted with the body contact pads, allowing low resistance conduction. Because of this,it was impossible to decouple the gate bias from the channel bias, which prevented further analysis. The leakage can be caused by many factors, but the main one in this case could be the Hall bar design, which was not ideal. It is important to note that only one of the two contact pads was short-circuited to the gate. This issue has been found in all structures, except for the one with short leg contacts (Figure 5.3b). Lastly, conduction through the substrate was observed, with a current flowing between contacts from different Hall bars. The resistivity of the Ge channel is much higher than that of the substrate. As both of them are in parallel with each other, most of the current flows in the substrate. This made it possible to measure a cross-conduction current, i.e. a current flowing between different devices, with a resistance of 2 kΩ.

The analysis has also been conducted at low temperatures ($T \sim 6$ K) only on the Hall bar without short-circuit. At low temperatures, the freeze-out of the carriers stops the substrate from conducting. When measuring with no bias applied, no current can flow in any direction, which means that both cross-conduction and channel conduction are impossible. Then a gate bias (both positive and negative) was applied to turn on channel conduction. a value of $V_g = \pm 8$ V has been reached without being able to populate the channel and decrease its resistivity. Only a small decrease of the resistivity was measured when applying a positive bias to the gate, suggesting that the substrate may be leading

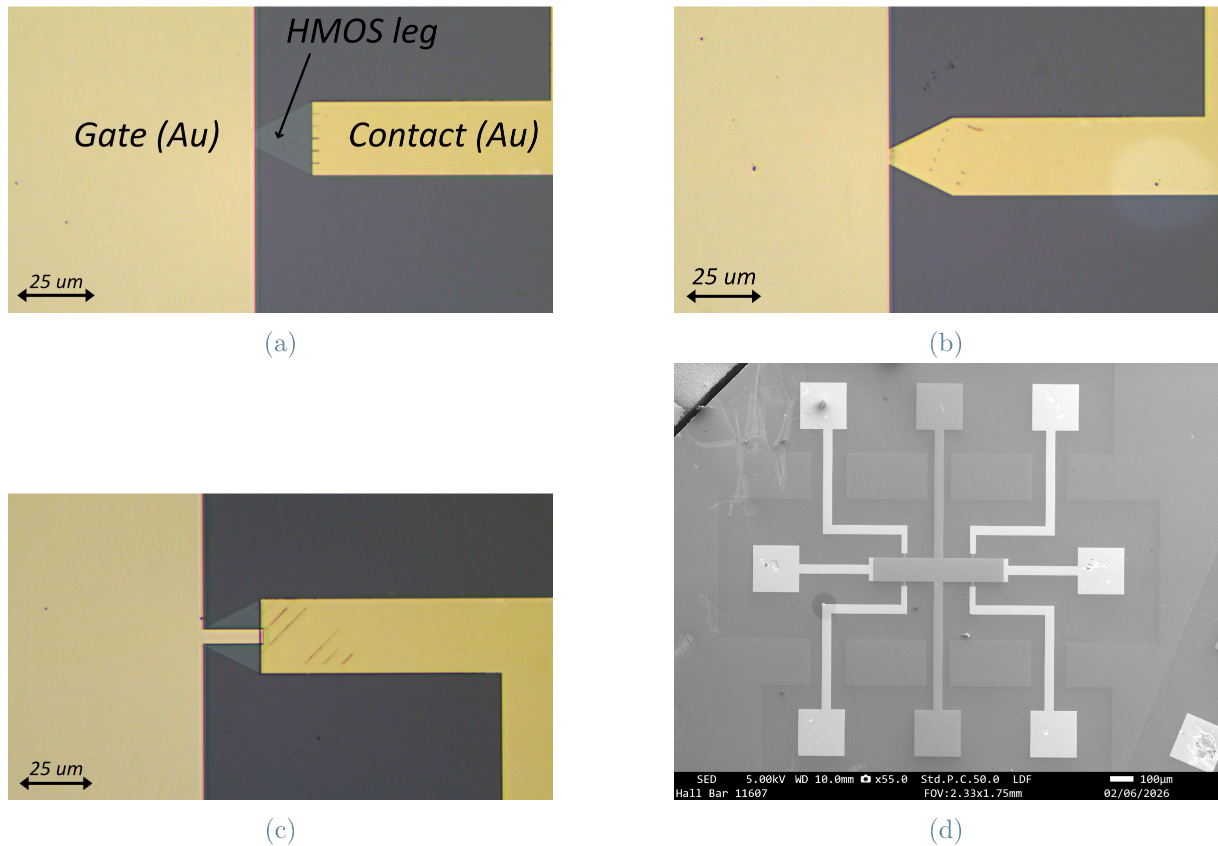

Figure 5.3: Different Hall bar structures analyzed in the 11607 sample. (a) A part of the Hall bar leg is left uncovered. (b) the leg contact is completely onto the Hall bar leg. (b) Only the gate metal is deposited onto a part of the legs to avoid freeze-out. (d) SEM image of the sample 11608 device.

the conduction.

The same measurements have been taken on the sample at $T \sim 25$ K and $T \sim 45$ K. The hypothesis was to set the temperature in a region where substrate conduction could be suppressed while still allowing the gate to induce carrier population in the channel. However, no noticeable current has been observed apart from substrate conduction, and there was no control from the gate over the channel.

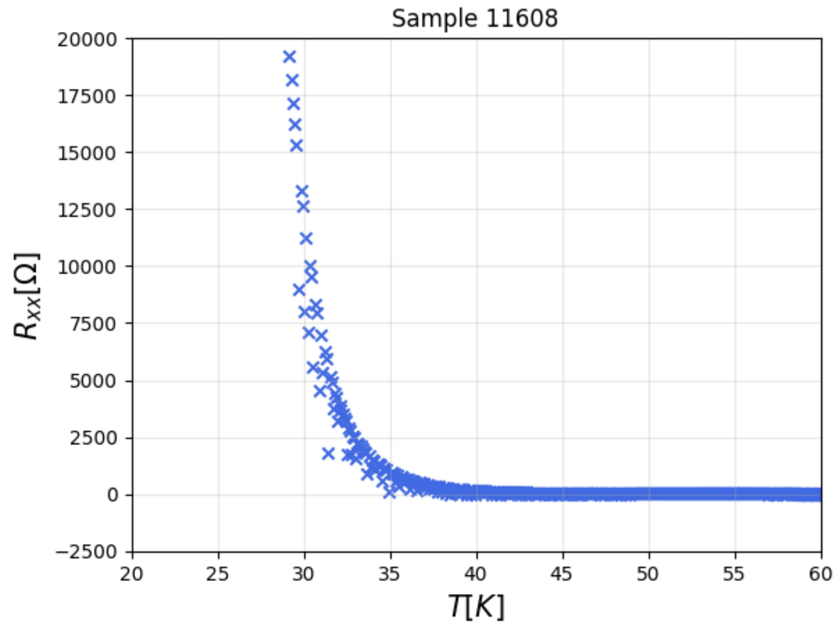

Figure 5.4: Resistance as a function of temperature as the sample was cooling down, measured between contact 2-3. An area around $T = 35K$ can be indicated as the freeze-out region of the conducting channel (in this case, the substrate).

5.0.2. 11608 sample

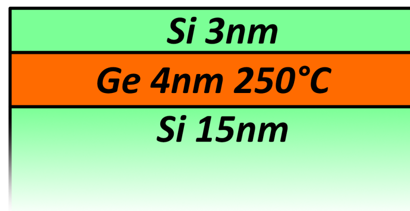

Figure 5.5: Stack of the 11608 sample channel region.

The 11608 sample is similar to the previous one, but with a channel grown at 250°C (Figure 5.5. Similar results have been obtained, with the additional problem that all devices presented a leakage with a resistance of $\sim 230\ \Omega$ between the channel and the gate (contacts 4-7). Again, applying a gate voltage did not influence the channel at all, so no low temperature analysis has been conducted in this case.

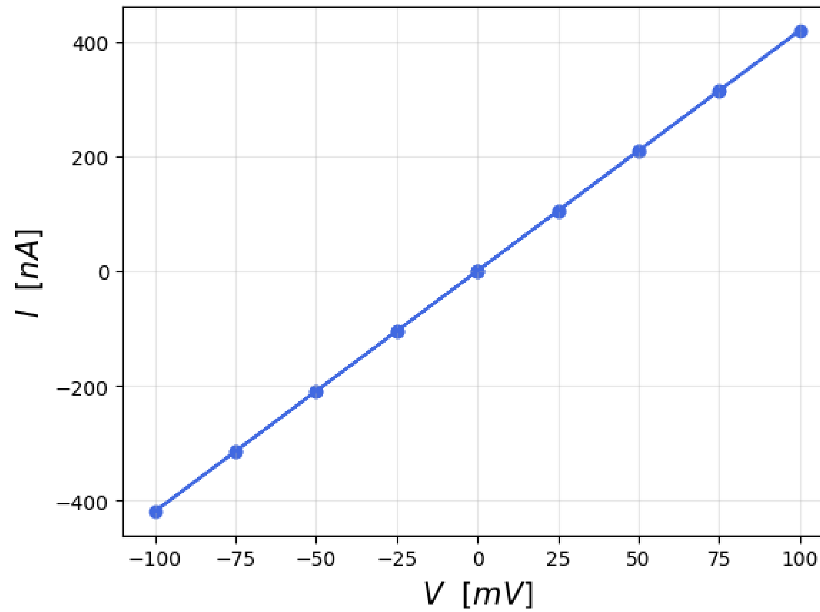

Figure 5.6: 11608 Hall bar gate leakage between contacts 4-7, represented in a $I(V)$ curve. One can see the perfect ohmic $I(V)$ line typical of metal conduction.

In general, very few valuable results have been obtained about the devices electrical properties. The conductivity of the Ge layer is so low that it is very hard to let it conduct without making a current flow through the substrate. However, the results could lead to future improvements in the design of the device and epitaxial stack.The next goal will be to investigate whether the conduction actually takes place in the Si substrate, with the Ge channel acting as a gate on top of it. Another option that will be explored is to deposit this epitaxial stack on top of highly intrinsic substrates ($\rho > 10$ kΩ·cm) to completely suppress substrate conduction and isolate the contribution of the germanium channel.

6 | Ge/SiGe HMOS Samples Analysis

6.0.1. 11585 Oxide no Gate

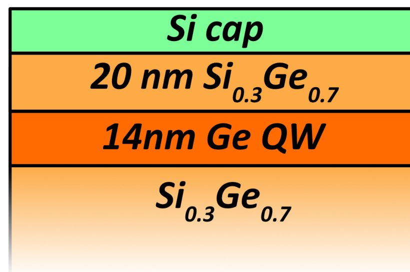

Figure 6.1: Stack of the 11585 channel region

The 11585 sample is characterized by a 14 nm Ge QW layer (Figure 6.1) and a plasma ALD process. At room temperature, the sample showed a body resistance of $\sim$ 38 kΩ, which was confirmed by a 4-probe measurement utilizing the leg contacts. Substrate conduction has also been found in the sample between contact 3 and contact 6 of two different devices, with a resistance of $\sim$ 80 kΩ.

When the temperature was reduced to 6 K, the device experiences a complete freeze-out of both the substrate conduction and the Ge QW. Conduction was not possible under these conditions and no gate was present to induce the population in the well. Similarly to 11607, it has been impossible to find a temperature to freeze-out the substrate while maintaining the conduction of the Ge QW. At the same time, the residual charges inside the oxide could not turn on conduction in the channel. This is an common effect in devices fabricated at ISTA, and is an important detail that need further characterization in the future.

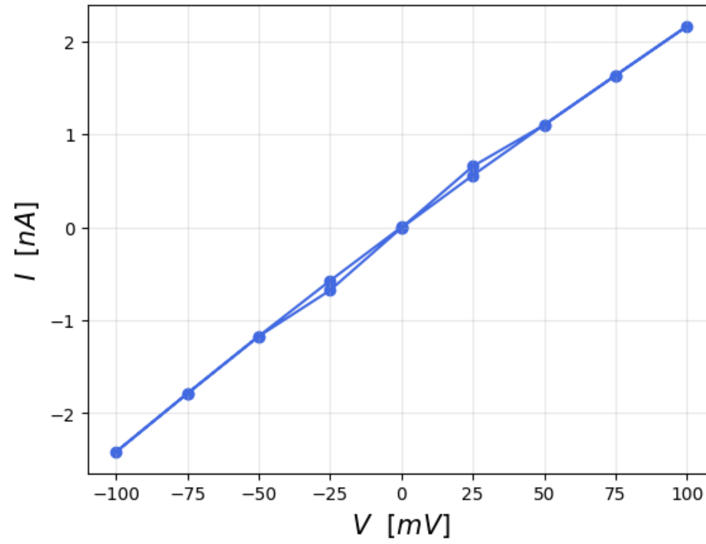

Figure 6.2: 11585 Hall bar body conduction (contact 1-4) represented in a $I(V)$ curve.

6.0.2. 11585 Gated

Sample 11585 has been gated, obtaining another degree of freedom, that being the gate bias. In this way, the high resistance Ge channel found in the previous analysis can be populated with holes, increasing the overall conductivity.

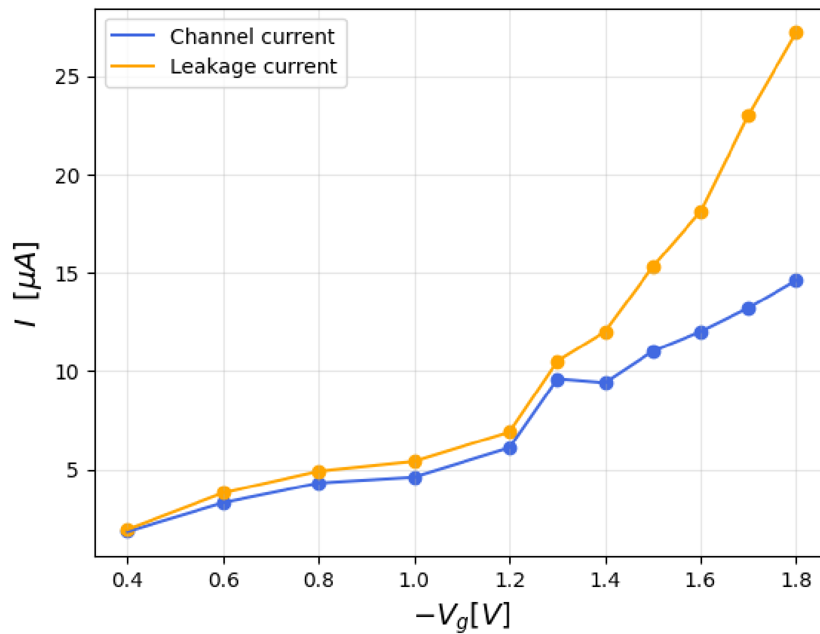

Figure 6.4: Channel current (contacts 1-4) and gate current (contacts 1-7) for different values of V_g. Initially, the channel current seems to follow the gate current, before they separate more for $V_g > -1.35$ V.

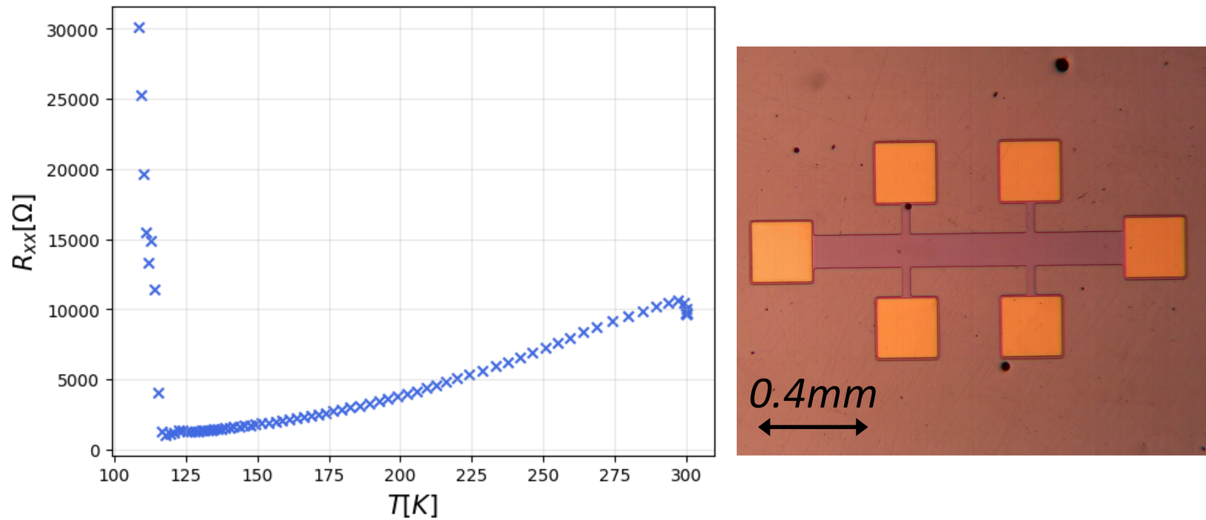

(a) 11585 Hall bar body conduction (contacts 1-4) represented in a $R(T)$ curve. The freeze out appears around 120 K.

(b) 11585 oxide no gate Hall bar optical image.

The sample was analyzed at 6 K by applying a bias to the channel and slowly increasing the gate bias to study the change in resistivity. Unfortunately, a leakage current was found to flow between the body contact and the gate contact, making the channel current reading impossible. Many attempts have been made to decouple the two currents, but no solution has been found. Furthermore, no resistivity measurement has been possible in the channel as a result of noise introduced by the much larger leakage current in the gate.

6.0.3. 11586 gated

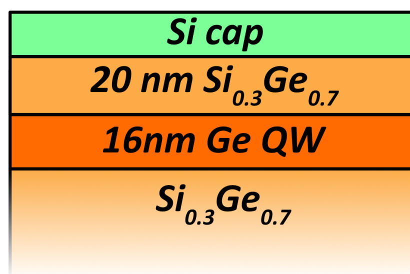

Figure 6.5: Stack of the 11586 channel region.

The analysis of 11586 has been conducted only on the gated structure. This choice has been taken for a few reasons. On one hand, one can expect the same behavior as the 11585, where no conduction was possible at low temperatures, and there has been no way to turn on the channel. On the other hand, if no V_g is applied to the gate, the device is virtually the same as an oxide-no-gate Hall bar.

Similar problems to the previous sample have been found in sample 11586. The sample was first measured at room temperature, where a leakage current was found to flow between the body contact and the gate contact. In this case, the $I(V_g)$ curve has been measured at $T = 300$ K (Figure 6.6), where it shows a more regular behavior than the previous sample at $T = 5.5$ K.

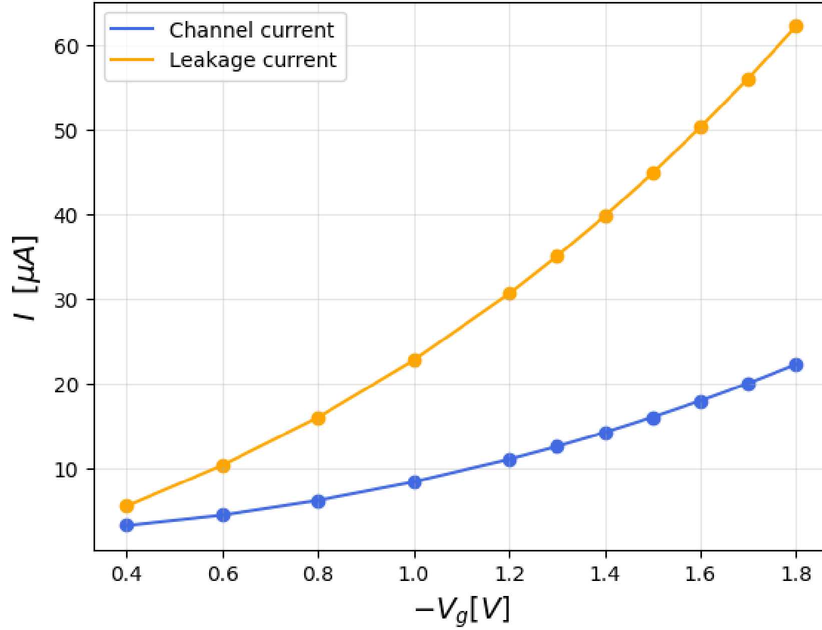

Figure 6.6: Channel current (contacts 1-4) and gate current (contacts 1-7) in sample 11586 at $T = 300$ K.

When the sample was inserted into the cryostat, the device lost contact with the measurement instruments preventing any $I(V_g)$ curve to be measured. The sample was then extracted from the cryostat and the failure will be analyzed in the future.

In the end, neither device was useful for extracting the figures of merit of the sample.

Conclusions

The scope of this work was to implement and test a Hall bar fabrication process and to characterize the devices manufactured at ISTA and Polifab.

The fabrication process has been tested for the first time at Polifab. Most of the fabrication steps have given the expected results and it has been proven that is possible for L-NESS to create its Hall bars directly at Polifab. Furthermore, critical steps have been found and characterized in order to improve them in further implementations.

Of the 260 nm target etching depth, only 120 nm have been removed. It is important to note that this difference should not cause any issue to the device, as the etching depth surpassed the Ge QW layer. However, it is still an important data to analyze for future development.

The strong gate leakage current found in the Polifab devices could be caused by the oxide not being able to separate the gate from the Hall bar. From Figure 4.10 in section 4.4, the Al_2O_3 layer seems perfectly conformal to the surface, as expected from an ALD process. However, subsequent fabrication steps could be the leading cause. In fact, the AZ 726 MIF developer used in the lithographic process for gate deposition contains Tetramethylammonium hydroxide (TMAH), a molecule that can etch Al_2O_3. This could create thinner regions in the oxide, damaging the MOS structure and preventing the isolation that the Al_2O_3 layer should provide. Nevertheless, it is important to note that to etch 20 nm of oxide, the development bath should be much longer than the one implemented in this work and it has not yet been proven that the TMAH is causing the leakage current.

Further studies on the characterization of the oxide onto simpler MOS devices are needed. Characterization instruments, such as SEM, Atomic Force Microscopy, ellipsometer, etc., could be useful to analyze the oxide layer and understand the leading cause of the issues. More samples are also needed to test and optimize the fabrication process so that L-NESS will be able to characterize its samples with an internal process flow.

Leakage was also found in most ISTA Hall bars, and there has been no influence from the gate onto the channel. The leakage is probably due to the Hall bar design or could be

caused by a fabrication error. The main concern in this matter is the oxide layer, which should isolate the gate from the Hall bar but failed to do so. However, when no leakage was present, the absence of control of the gate onto the channel could have been caused by the freeze-out of the Hall bar legs, which were not covered by the gate in the design.

Discussions with members of the ISTA group will provide the necessary feedback to understand how to solve the issues. On the L-NESS side, further depositions employing ultra-intrinsic substrates are needed to decouple the two conductive channels represented by thin Ge and the substrate.

Bibliography

[1] Daniel Jirovec, Andrea Hofmann, Andrea Ballabio, Philipp M. Mutter, Giulio Tavani, Marc Botifoll, Alessandro Crippa, Josip Kukucka, Oliver Sagi, Frederico Martins, Jaime Saez-Mollejo, Ivan Prieto, Maksim Borovkov, Jordi Arbiol, Daniel Chrastina, Giovanni Isella, and Georgios Katsaros. A singlet-triplet hole spin qubit in planar Ge. *Nature Materials*, 20(8):1106–1112, 2021.

[2] Maksym Myronov, Jan Kycia, Philip Waldron, Weihong Jiang, Pedro Barrios, Alex Bogan, Peter Coleridge, and Sergei Studenikin. Holes outperform electrons in group iv semiconductor materials. *Small Science*, 3(4):2200094, 2023.

[3] R. J. P. Lander, M. J. Kearney, A. I. Horrell, E. H. C. Parker, P. J. Phillips, and T. E. Whall. On the low-temperature mobility of holes in gated oxide Si/SiGe heterostructures. *Semiconductor Science and Technology*, 12(9):1064, 1997.

[4] D. Chrastina, J. P. Hague, and D. R. Leadley. Application of Bryan's algorithm to the mobility spectrum analysis of semiconductor devices. *Journal of Applied Physics*, 94(10):6583–6590, 2003.

[5] Stefano Calcaterra. Germanium quantum wells for semiconductor qubits. Tesi di laurea magistrale, Politecnico di Milano, Milano, Italy, 2021.

[6] Mario Lodari, Nico Hendrickx, William Lawrie, Tzu kan Hsiao, Lieven Vandersypen, Amir Sammak, Menno Veldhorst, and Giordano Scappucci. Low percolation density and charge noise with holes in germanium. *Mater. Quantum Technol.*, 1(1):011002, 2021.

[7] A. M. J. Zwerver, F. van Riggelen, N. W. Hendrickx, W. I. L. Lawrie, M. Russ, S. G. J. Philips, R. van Veldhoven, J. M. Boter, M. A. Verheijen, L. M. K. Vandersypen, and G. Scappucci. Impact of heterostructure design on the performance of silicon spin qubits. *Nature Reviews Materials*, 2024.

[8] Alberto Mistroni, Marco Lisker, Yuji Yamamoto, Wei-Chen Wen, Fabian Fidorra, Henriette Tetzner, Laura K. Diebel, Lino Visser, Spandan Anupam, Vincent Mourik, Lars R. Schreiber, Hendrik Bluhm, Dominique Bougeard, Marvin H. Zoellner, Gio-

vanni Capellini, and Felix Reichmann. High yield, low disorder Si/SiGe heterostructures for spin qubit devices manufactured in a BiCMOS pilot line. *Applied Physics Letters*, 127(8):083503, 08 2025.

[9] Yu-Cheng Li, Che-Hao Chang, Yu-Jui Wu, Chen-Yao Liao, and Jiun-Yun Li. Design guidelines for Si metal–oxide–semiconductor and Si/SiGe heterostructure quantum dots for spin qubits. *Applied Physics Letters*, 126(6):063502, February 2025.

[10] John M. Martinis. Superconducting phase qubits. In *Quantum Computing in Solid State Systems: Les Houches Session LXXIX*, pages 117–166. Springer, 2004. Lecture notes from Les Houches Summer School.

[11] Pieter Kok, William J. Munro, Kae Nemoto, Timothy C. Ralph, Jonathan P. Dowling, and Gerard J. Milburn. Linear optical quantum computing with photonic qubits. *Reviews of Modern Physics*, 79(1):135–174, 2007.

[12] Tian Zhong, Yichen Wang, Zhiwei Li, Yuxuan Zhang, Ming Chen, Xiaoyang Li, Zhi Zhou, Jian Wang, and Qiang Zhang. Realization of a programmable multipurpose photonic quantum memory with over-thousand qubit manipulations. *Nature Photonics*, 2024.

[13] Guangyu Zhang, Huaijin Zhang, and Zhang-Qi Yin. Scalable universal quantum gates between nitrogen-vacancy centers in levitated nanodiamond arrays. *Phys. Rev. A*, 112(032611), 2025. DOI: 10.1103/zgk4-1556.

[14] J. R. Petta, T. Struck, M. J. Gullans, J. M. Taylor, G. Burkard, L. M. K. Vandersypen, J. Stehlik, D. M. Zajac, S. Foletti, and E. I. Rashba. Semiconductor spin qubits. *Reviews of Modern Physics*, 95(2):025003, 2023.

[15] J. R. Petta, A. C. Johnson, J. M. Taylor, E. A. Laird, A. Yacoby, M. D. Lukin, C. M. Marcus, M. P. Hanson, and A. C. Gossard. Coherent manipulation of coupled electron spins in semiconductor quantum dots. *Science*, 309(5744):2180–2184, 2005.

[16] M. Veldhorst, C. H. Yang, J. C. C. Hwang, W. Huang, J. P. Dehollain, J. T. Muhonen, S. Simmons, A. Laucht, F. E. Hudson, K. M. Itoh, A. Morello, and A. S. Dzurak. A two-qubit logic gate in silicon. *Nature*, 526:410–414, 2015.

[17] E. Kawakami, P. Scarlino, D. R. Ward, F. R. Braakman, D. E. Savage, M. G. Lagally, M. Friesen, S. N. Coppersmith, M. A. Eriksson, and L. M. K. Vandersypen. Electrical control of a long-lived spin qubit in a Si/SiGe quantum dot. *Nature Nanotechnology*, 9:666–670, 2014.

[18] V. Umansky, R. de Picciotto, and M. Heiblum. Extremely high mobility two-dimensional electron system. *Applied Physics Letters*, 71(5):683–685, 1997.

[19] A. C. Churchill, D. J. Robbins, D. J. Wallis, N. Griffin, D. J. Paul, and A. J. Pidduck. High-mobility two-dimensional electron gases in Si/SiGe heterostructures on relaxed SiGe layers grown at high temperature. *Semiconductor Science and Technology*, 12(8):943, 1997.

[20] T. Onabe, H. Sakaki, and J. Yoshino. High-mobility two-dimensional electron gas in modulation-doped InAlAs/InGaAs heterostructures. *Applied Physics Letters*, 43(10):984–986, 1983.

[21] Y. H. Zhang, L. Tapfer, and K. Ploog. High electron mobility in modulation-doped $Ga_xIn_{1-x}As/Al_yIn_{1-y}As$ heterostructures with highly strained AlInAs grown by molecular beam epitaxy. *Semiconductor Science and Technology*, 5(7):803, 1990.

[22] Arianna Nigro, Eric Jutzi, Nicolas Forrer, Andrea Hofmann, Gerard Gadea, and Ilaria Zardo. High quality Ge layers for Ge/SiGe quantum well heterostructures using chemical vapor deposition. *Physical Review Materials*, 8(6):066201, 2024.

[23] Yi Huang and Sankar Das Sarma. Understanding disorder in silicon quantum computing platforms: Scattering mechanisms in Si/SiGe quantum wells. *Physical Review B*, 109(12):125405, March 2024.

[24] Stefan Birner, Tobias Zibold, Till Andlauer, Tillmann Kubis, Matthias Sabathil, Alex Trellakis, and Peter Vogl. nextnano: General purpose 3-d simulations. *IEEE Transactions on Electron Devices*, 54(9):2137–2142, 2007.

[25] D. Laroche, S.-H. Huang, Y. Chuang, J.-Y. Li, C. W. Liu, and T. M. Lu. Magnetotransport analysis of an ultra-low-density two-dimensional hole gas in an undoped strained Ge/SiGe heterostructure. *Applied Physics Letters*, 108(23):233504, 2016.

[26] M. Lodari, A. Tosato, D. Sabbagh, M. A. Schubert, G. Capellini, A. Sammak, M. Veldhorst, and G. Scappucci. Light effective hole mass in undoped Ge/SiGe quantum wells. *Phys. Rev. B*, 100:041304, Jul 2019.

[27] Davide Costa, Lucas E. A. Stehouwer, Yi Huang, Sara Martí-Sánchez, Davide Degli Esposti, Jordi Arbiol, and Giordano Scappucci. Reducing disorder in Ge quantum wells by using thick SiGe barriers. *Applied Physics Letters*, 125(22):222104, 2024.

[28] Maksym Myronov, Alex Bogan, and Sergei Studenikin. Hole mobility in compres-

sively strained germanium on silicon exceeds 7×10^6 $\mathrm{cm^2V^{-1}s^{-1}}$. *Materials Today*, 90:314–321, 2025.

[29] G. Abstreiter. Electronic properties of Si/SiGe/Ge heterostructures. *Physica Scripta*, T68:61–71, 1996.

[30] M. Virgilio and G. Grosso. Type-I alignment and direct fundamental gap in SiGe based heterostructures. *Journal of Physics: Condensed Matter*, 18(3), 2006.

[31] F. F. Fang and W. E. Howard. Negative field-effect mobility on (100) Si surfaces. *Physical Review Letters*, 16(18):797–799, May 1966.

[32] Shiming Zheng, E. S. Khramtsov, and I. V. Ignatiev. Effect of electric field on excitons in wide quantum wells, 2024.

[33] D. Chrastina, B. Rössner, G. Isella, H. von Känel, J. P. Hague, T. Hackbarth, H.-J. Herzog, K.-H. Hieber, and U. König. LEPECVD – a production technique for SiGe MOSFETs and MODFETs. In Ehrenfried Zschech, Caroline Whelan, and Thomas Mikolajick, editors, *Materials for Information Technology: Engineering Materials and Processes*, pages 17–29. Springer, London, UK, 2005.

[34] Abel Thayil, Lasse Ermoneit, and Markus Kantner. Theory of valley splitting in Si/SiGe spin qubits: Interplay of strain, resonances, and random alloy disorder. *Phys. Rev. B*, 112:115303, Sep 2025.

[35] Patrick Del Vecchio and Oussama Moutanabbir. Light-hole spin confined in germanium. *Physical Review B*, 110(4), July 2024.

[36] Thomas Ihn. *Semiconductor Nanostructures: Quantum States and Electronic Transport*. OUP Oxford, 2009.

[37] L. A. Terrazos, E. Marcellina, Zhanning Wang, S. N. Coppersmith, Mark Friesen, A. R. Hamilton, Xuedong Hu, Belita Koiller, A. L. Saraiva, Dimitrie Culcer, and Rodrigo B. Capaz. Theory of hole-spin qubits in strained germanium quantum dots. *Physical Review B*, 103(12), March 2021.

[38] Tianli Feng, Bo Qiu, and Xiulin Ruan. Coupling between phonon-phonon and phonon-impurity scattering: A critical revisit of the spectral Matthiessen's rule. *Physical Review B*, 92(23):235206, 2015.

[39] J. P. Harrang, R. J. Higgins, R. K. Goodall, P. R. Jay, M. Laviron, and P. Delescluse. Quantum and classical mobility determination of the dominant scattering mechanism

in the two-dimensional electron gas of an AlGaAs/GaAs heterojunction. *Physical Review B*, 32(12):8126–8135, 1985.

[40] Gerald Bastard. *Wave Mechanics Applied to Semiconductor Heterostructures*. Monographies de physique. Les Editions de Physique; Wiley-Interscience, Les Ulis, France; New York, USA, 1988.

[41] T. Ando, A. B. Fowler, and F. Stern. Electronic properties of two-dimensional systems. *Reviews of Modern Physics*, 54(2):437–672, 1982.

[42] T. Tschirky, S. Mueller, Ch. A. Lehner, S. Fält, T. Ihn, K. Ensslin, and W. Wegscheider. Scattering mechanisms of highest-mobility InAs/$Al_xGa_{1-x}Sb$ quantum wells. *Physical Review B*, 95(11):115304, 2017.

[43] Alex M. Ganose, Junsoo Park, and Anubhav Jain. The temperature-dependence of carrier mobility is not a reliable indicator of the dominant scattering mechanism. *arXiv preprint arXiv:2210.01746*, 2022.

[44] P. T. Coleridge. Small-angle scattering in two-dimensional electron gases. *Physical Review B*, 44(8):3793–3801, 1991.

[45] K. Hirakawa and H. Sakaki. Interface roughness scattering in semiconductor quantum wells. *Semiconductor Science and Technology*, 19(2):S1–S5, 2004.

[46] Saumitra R. Mehrotra, Abhijeet Paul, and Gerhard Klimeck. Atomistic approach to alloy scattering in $Si_{1-x}Ge_x$. *arXiv preprint arXiv:1102.4805*, 2011.

[47] Mildred Dresselhaus, Gene Dresselhaus, Stephen B. Cronin, and Antonio Gomes Souza Filho. *Solid State Properties: From Bulk to Nano*. Graduate Texts in Physics. Springer, 2018.

[48] L. A. Tracy, E. H. Hwang, K. Eng, G. A. Ten Eyck, E. P. Nordberg, K. Childs, M. S. Carroll, M. P. Lilly, and S. Das Sarma. Observation of percolation-induced two-dimensional metal-insulator transition in a Si MOSFET. *Physical Review B*, 79(23), 2009.

[49] S. V. Kravchenko and M. P. Sarachik. Metal-insulator transition in two-dimensional electron systems. *Reports on Progress in Physics*, 67(1):1–44, 2004.

[50] S. Das Sarma and E. H. Hwang. Charged impurity-scattering-limited low-temperature resistivity of low-density silicon inversion layers. *Physical Review Letters*, 83:164–167, 1999.

[51] Ronald J. Pieper and Sherif Michael. An exact analysis for freeze-out and exhaustion in single impurity semiconductors. In *ASEE 2005 Annual Conference*, 2005.

[52] W. A. Beck and J. R. Anderson. Determination of electrical transport properties using a novel magnetic field-dependent hall technique. *Journal of Applied Physics*, 62(2):541–554, 1987.

[53] Joseph E. Dill, Chuan F. C. Chang, Debdeep Jena, and Huili Grace Xing. Two-carrier model-fitting of Hall effect in semiconductors with dual-band occupation: A case study in GaN two-dimensional hole gas. *Journal of Applied Physics*, 137(2):025702, 2025.

[54] Carl A Kukkonen and Pierre F. Maldague. Electron-electron scattering: Hall coefficient and magnetoresistance. *Phys. Rev. B*, 19:2394–2397, 1979.

[55] Victor Ciupina, Gabriela Prodan, Gheorghe I. Rusu, Constantin Gheorghies, and Eugen Vasile. The influence of heat treatment on the electrical conductivity of antimony trioxide thin films. *Journal of Optoelectronics and Advanced Materials*, 4(4):907–912, 2002.

[56] M. Q. Dong, Zhi-Xin Guo, and X. R. Wang. Anisotropic magnetoresistance due to magnetization-dependent spin-orbit interactions. *Phys. Rev. B*, 108:L020401, 2023.

[57] Xian-Peng Zhang, Run-Wu Zhang, Xiaolong Fan, Wanxiang Feng, Xiangrong Wang, and Yugui Yao. A theory of anisotropic magnetoresistance in altermagnets and its applications. *Phys. Rev. Lett.*, 135:266706, 2025.

[58] Neil W. Ashcroft and N. David Mermin. Chapter 14: Energy bands. In *Solid State Physics*, pages 217–224. Holt, Rinehart and Winston, 1976.

[59] A. Poux, Z. R. Wasilewski, K. J. Friedland, R. Hey, K. H. Ploog, R. Airey, P. Plochocka, and D. K. Maude. A microscopic model for the magnetic field driven breakdown of the dissipationless state in the integer and fractional quantum hall effect. *arXiv preprint arXiv:1609.00485*, 2016.

[60] M. Z. Hasan and C. L. Kane. Colloquium: Topological insulators. *arXiv preprint arXiv:0804.2546*, 2008.

[61] P. T. Coleridge, A. S. Sachrajda, and P. Zawadzki. Weak localization, interaction effects, and the metallic phase in p-SiGe. *Phys. Rev. B*, 65:125328, 2002.

[62] Ryota Akiyama, Kazuki Sumida, Satoru Ichinokura, Ryosuke Nakanishi, Akio Kimura, Konstantin A. Kokh, Oleg E. Tereshchenko, and Shuji Hasegawa. Shub-

nikov–de Haas oscillations in p and n-type topological insulator $(Bi_xSb_{1-x})_2Te_3$. *Journal of Physics: Condensed Matter*, 30(26):265001, 2018.

[63] Devendra Kumar and Archana Lakhani. Observation of three-dimensional Dirac semimetal state in topological insulator Bi_2Se_3. *Physica Status Solidi (RRL) – Rapid Research Letters*, 9(11):636–640, 2015. Also available as arXiv preprint arXiv:1504.08328.

[64] Sean A. Hartnoll and Diego M. Hofman. Generalized Lifshitz–Kosevich scaling at quantum criticality from the holographic correspondence. *Physical Review B*, 81(15), April 2010.

[65] Jelena Klinovaja and Daniel Loss. Topological edge states and fractional quantum Hall effect from umklapp scattering. *Phys. Rev. Lett.*, 111:196401, Nov 2013.

[66] Horst L. Stormer. Nobel lecture: The fractional quantum Hall effect. *Reviews of Modern Physics*, 71:875–889, Jul 1999.

[67] Karol I. Wysokinski. Integer and fractional quantum Hall effects. *European Journal of Physics*, 21(6):p. 535–548, Nov 2000.

[68] Yang Liu, S. Hasdemir, D. Kamburov, A. L. Graninger, M. Shayegan, L. N. Pfeiffer, K. W. West, K. W. Baldwin, and R. Winkler. Even-denominator fractional quantum Hall effect at a Landau level crossing. *Phys. Rev. B*, 89:165313, Apr 2014.

[69] N. B. Wilding and A. D. Bruce. Density fluctuations and field mixing in the critical fluid. *Journal of Physics: Condensed Matter*, 8(46), 1996.

[70] Amir Sammak, Diego Sabbagh, Nico W. Hendrickx, Mario Lodari, Brian Paquelet Wuetz, Alberto Tosato, LaReine Yeoh, Monica Bollani, Michele Virgilio ad Markus Andreas Schubert, Peter Zaumseil, Giovanni Capellini, Menno Veldhorst, and Giordano Scappucci. Shallow and undoped germanium quantum wells: A playground for spin and hybrid quantum technology. *Adv. Funct. Mater.*, 2019:1807613, 2019.

[71] James D. Plummer and Peter B. Griffin. *Integrated Circuit Fabrication: Science and Technology.* Cambridge University Press, Cambridge, UK, 2024.

[72] C. Rosenblad, H. von Känel, M. Kummer, A. Dommann, and E. Müller. A plasma process for ultrafast deposition of SiGe graded buffer layers. *Applied Physics Letters*, 76(4):427–429, 2000.

[73] V. Aubry, F. Meyer, R. Laval, C. Clerc, P. Warren, and D. Dutartre. Thermal stability of W on RTCVD $Si_{1-x}Ge_x$ films. *Appl. Surf. Sci.*, 73:285–289, 1993.